nature metabolism

Article

https://doi.org/10.1038/s42255-023-00838-3

Targeting the TCA cycle can ameliorate widespread axonal energy deficiency in neuroinflammatory lesions

Received: 19 March 2022

Accepted: 5 June 2023

Published online: 10 July 2023

Check for updates

Yi-Heng Tai[1,2,3], Daniel Engels[1,2], Giuseppe Locatelli[1,2,11], Ioanna Emmanouilidis[1,2,3], Caroline Fecher[3,4,12], Delphine Theodorou[1,2], Stephan A. Müller[4,5], Simon Licht-Mayer[6], Mario Kreutzfeldt[7], Ingrid Wagner[7], Natalia Prudente de Mello[8], Sofia-Natsouko Gkotzamani[1,2], Laura Trovò[3], Arek Kendirli[1,2], Almir Aljović[1,2], Michael O. Breckwoldt[1,2,3,13], Ronald Naumann[9], Florence M. Bareyre[1,2,10], Fabiana Perocchi[3,8,10], Don Mahad[6], Doron Merkler[7], Stefan F. Lichtenthaler[4,5,10], Martin Kerschensteiner[1,2,10,14] ✉ & Thomas Misgeld[3,4,10,14] ✉

Inflammation in the central nervous system can impair the function of neuronal mitochondria and contributes to axon degeneration in the common neuroinflammatory disease multiple sclerosis (MS). Here we combine cell-type-specific mitochondrial proteomics with in vivo biosensor imaging to dissect how inflammation alters the molecular composition and functional capacity of neuronal mitochondria. We show that neuroinflammatory lesions in the mouse spinal cord cause widespread and persisting axonal ATP deficiency, which precedes mitochondrial oxidation and calcium overload. This axonal energy deficiency is associated with impaired electron transport chain function, but also an upstream imbalance of tricarboxylic acid (TCA) cycle enzymes, with several, including key rate-limiting, enzymes being depleted in neuronal mitochondria in experimental models and in MS lesions. Notably, viral overexpression of individual TCA enzymes can ameliorate the axonal energy deficits in neuroinflammatory lesions, suggesting that TCA cycle dysfunction in MS may be amendable to therapy.

MS is a common neurological disease in which central nervous system (CNS) inflammation results in myelin loss and progressive neurodegeneration. While the importance of such neurodegenerative processes for long-term disability of patients with MS is well established[1–3], the mechanistic links between CNS inflammation and neurodegeneration remain to be resolved. Emerging evidence from patients with MS and the corresponding animal models indicates that neuronal mitochondria could be critical hubs that render inflammatory signals into neurodegenerative consequences. This concept is not only supported by the essential function of mitochondria in neuronal energy homeostasis[4], but also by previous studies showing (1) that damaged mitochondria accumulate in axons located in experimental and human neuroinflammatory lesions[5–7]; (2) that neuronal mitochondria acquire DNA deletions over the course of the disease[8]; and (3) that such inflammation-induced mitochondrial damage impairs electron transport chain (ETC) function[2,9].

Mitochondrial damage could thus be initiated already in the highly inflamed lesions of early MS and then further amplify over the course of the disease. This process would provide a link not only between inflammation and neurodegeneration, but also between initial relapsing–remitting and later progressive pathology[2,9]. As a result of these insights, mitochondria have emerged as a promising therapeutic

A full list of affiliations appears at the end of the paper. ✉e-mail: martin.kerschensteiner@med.uni-muenchen.de; thomas.misgeld@tum.de

target to prevent neurodegeneration throughout the disease course of MS. Unfortunately, so far, such strategies have failed to provide robust clinical benefits, at least in large clinical trials[10]. One of the reasons underlying this failure is that our understanding of how the molecular machinery and functional capability of mitochondria is impaired in neuroinflammatory lesions is still incomplete. Moreover, most studies so far have focused on ETC impairments[8,11], which might be hard to target therapeutically given the complex structure of the underlying macromolecular complexes and their genetics.

Here we apply new in vivo imaging strategies combined with selective ex vivo proteomic analysis of neuronal mitochondria in a murine MS model (experimental autoimmune encephalomyelitis; EAE) to investigate the molecular underpinnings and functional consequences of inflammation-induced mitochondrial pathology. We reveal that widespread axonal ATP deficiency is initiated in acute neuroinflammatory lesions and persists in the chronic disease stage. These bioenergetic deficits precede mitochondrial redox or calcium dyshomeostasis. Selective *MitoTag*-based proteomic analysis of neuronal mitochondria isolated from acute and chronic EAE spinal cords instead revealed an imbalance of critical TCA cycle enzymes, with a prominent loss of several enzymes, including isocitrate dehydrogenase 3 (Idh3) and malate dehydrogenase 2 (Mdh2). Notably, the depletion of these key TCA cycle enzymes in neuronal mitochondria is also apparent in human MS lesions. Finally, we show that viral gene therapy, overexpressing the catalytic subunit of Idh3 or Mdh2, can partially reverse axonal ATP deficits in neuroinflammatory lesions. Our study thus provides a refined understanding of how the molecular composition of neuronal mitochondria changes in response to neuroinflammation. We identify the depletion of TCA cycle enzymes as a critical mediator of the axonal energy crisis that occurs in neuroinflammatory lesions, thus defining a potential target for therapeutic intervention.

Results

Pervasive axonal ATP deficits emerge early in EAE lesions

As ATP production is a central function of mitochondria that is key in axons[12], we established an in vivo imaging approach to record the ATP/ADP ratio of individual axons in neuroinflammatory lesions. We generated *Thy1*-PercevalHR mice, in which neurons express PercevalHR, a genetically encoded excitation ratiometric biosensor that monitors the cytoplasmic ATP/ADP ratio[13]. Histological characterization confirmed the targeting of the sensor to a broad range of neuronal populations in the brain and spinal cord (Extended Data Fig. 1a). To assess whether the sensor was indeed capable of recording ATP deficits in spinal axons, we pharmacologically interfered with ATP production and recorded the ATP/ADP ratio by measuring fluorescence emission after excitation at 950 and 840 nm using in vivo two-photon microscopy. Application of either the glycolysis inhibitor iodoacetic acid (IAA) (10 mM) or the mitochondrial uncoupling agent carbonyl cyanide m-chlorophenyl hydrazone (CCCP) (100 µM) to the exposed dorsal spinal cord resulted in a swift reduction of the ATP/ADP ratio in spinal axons (Extended Data Fig. 1b,c).

To assess the emergence of axonal energy deficits in neuroinflammatory lesions, we next induced EAE, a widely used model of MS, by immunizing *Thy1*-PercevalHR mice with myelin-oligodendrocyte glycoprotein (MOG). In vivo two-photon imaging then allowed us to record the ATP/ADP ratio in axons that cross through a neuroinflammatory lesion and at the same time to stage axonal morphology, a predictor of axonal fate as we established previously[6]. We found widespread axonal ATP deficits that not only affected axons that were swollen (stage 1 axons) or fragmented (stage 2) and had hence already entered the focal axonal degeneration (FAD) process[6,14], but also morphologically normal axons (stage 0; Fig. 1a–e). Axons were not only showing a reduced ATP/ADP ratio in acute lesions (analyzed 2 or 3 d after EAE symptom onset), but ATP deficits persisted in axons of all FAD stages in chronic lesions (analyzed an additional 20 d later; Fig. 1d,e). To explore, whether neurons in their entirety lacked ATP or whether this was a local axonal deficit, we traced individual sensory axons from the lesion back into the dorsal roots, where neuroinflammation is typically not present in EAE. Comparing the ATP/ADP ratios in the same axons close to and far from the intraspinal lesion area revealed that ATP deficits were most pronounced at the sites of CNS inflammation (Fig. 1f,g). To independently corroborate these results with another biosensor, we intravenously injected recombinant adeno-associated virus (rAAV.PHP.eB) to neuronally express ATeam, a fluorescence resonance energy transfer (FRET)-based ATP level sensor (rAAV.hSyn:ATeam)[15]. In vivo imaging of ATeam-expressing axons confirmed a pervasive reduction in ATP availability in axons within spinal EAE lesions (Extended Data Fig. 2a–d), whereas in converse, a pH biosensor (SypHer3s; rAAV.hSyn:SypHer3s)[16], failed to identify changes in axoplasmic pH that could interfere with the PercevalHR and ATeam sensors (Extended Data Fig. 2e). Hence, our data indicate that axons in neuroinflammatory lesions exist in a sustained state of reduced ATP availability, a finding that is in line with the localized accumulation and damage of mitochondria that we previously described in spinal cord lesions of the same MS model[6,17].

ATP deficits precede mitochondrial redox and Ca^{2+} changes

Oxidative stress to axons had previously been proposed as a mediator of mitochondrial damage in neuroinflammatory lesions[1–3,9,18]. Thus, we set out to determine whether and when an altered redox status of axonal mitochondria would emerge in relation to the onset of neuroinflammation-induced ATP deficit. We used *Thy1*-mitoGrx-roGFP mice, which allow recording of the glutathione redox potential in neuronal mitochondria, as we previously established[19]. After crossing these redox reporter mice to *Thy1*-OFP mice[20] to allow staging of axonal morphology, we induced EAE and performed ratiometric in vivo confocal imaging using single-photon excitation at 405 and 488 nm at the peak of acute disease symptoms. An oxidative shift in mitochondrial redox state was only apparent in fragmented (stage 2) axons, whereas mitochondria in normal-appearing (stage 0) and swollen (stage 1) axons were unaltered compared to control axons in a healthy spinal cord (Fig. 2a–d). This is notable, as the analysis of individual mitochondria confirmed that damage-related mitochondrial shape changes, such as rounding up (reduced shape factor), are already present at the onset of FAD (Fig. 2e)[6,17]. Decompensated mitochondrial redox stress thus seems to be a late event during inflammatory axon degeneration and affects

Fig. 1 | Early and pervasive axonal ATP deficits in EAE lesions. a, Experimental design for axonal ATP/ADP ratio ($[ATP/ADP]_{axon}$) measurements in EAE. **b**, Maximum intensity projections of in vivo multi-photon image stacks of spinal cord axons of control (left) and acute EAE (right) in *Thy1*-PercevalHR mice. Grayscale look-up table (LUT; λ_{ex} 950 nm) (top). Ratiometric $[ATP/ADP]_{axon}$ LUT (λ_{ex} ratio 950 nm:840 nm) (bottom). L, low; H, high. **c**, Details from **b**. $[ATP/ADP]_{axon}$ images of control axon in healthy spinal cord and normal-appearing, swollen and fragmented axons in acute EAE (top to bottom). **d**, Spinal cord axons during chronic EAE shown as in **b**. **e**, $[ATP/ADP]_{axon}$ of single axons in healthy and EAE mice normalized to mean of controls (magenta: axons after CCCP, 100 µM; mean ± s.e.m.; 246 axons from six control, 272 axons from four EAE, acute and 522 axons from six EAE, chronic mice; compared by Kruskal–Wallis and Dunn's multiple comparison test; values ≥ 1.5 are lined up on the '≥1.5' dashed line). **f**, $[ATP/ADP]_{axon}$ gradient in a dorsal root axon traced through a lesion using in vivo multi-photon imaging. Traced axon pseudo-colored yellow, running from root at top left to the lesion center at lower right, superimposed on full volume projection, grayscale LUT, λ_{ex} 950 nm (left). Boxes indicate locations of high-resolution stacks. Details showing the $[ATP/ADP]_{axon}$ gradient between locations far from (1) versus close to the lesion (3) (right). LUTs as in **b**. **g**, Paired analysis of $[ATP/ADP]_{axon}$ far versus close to the lesion (n = 22 axons from three EAE mice; two-tailed, paired t-test; normalized to control). Scale bars, 25 µm in **b**, also applied to **d**; 10 µm in **c** and **f** (right); 100 µm in **f** (left). ****$P < 0.001$. See source data for individual data points and further statistical parameters. Illustration created with BioRender.

https://doi.org/10.1038/s42255-023-00838-3

only a small proportion of non-fragmented axons in neuroinflammatory lesions. Oxidative mitochondrial damage per se is hence unlikely to underlie the widespread axonal ATP deficits in EAE.

In addition to oxidative damage, calcium overload was proposed to mediate mitochondrial dysfunction[1,21]. To monitor calcium handling of axonal mitochondria in vivo, we generated a transgenic reporter mouse line that expresses the ratiometric calcium sensor Twitch2b[22] selectively in neuronal mitochondria. Histological characterization of these *Thy1*-mitoTwitch2b mice confirmed widespread sensor expression in CNS neurons. Moreover, induction of localized laser lesions

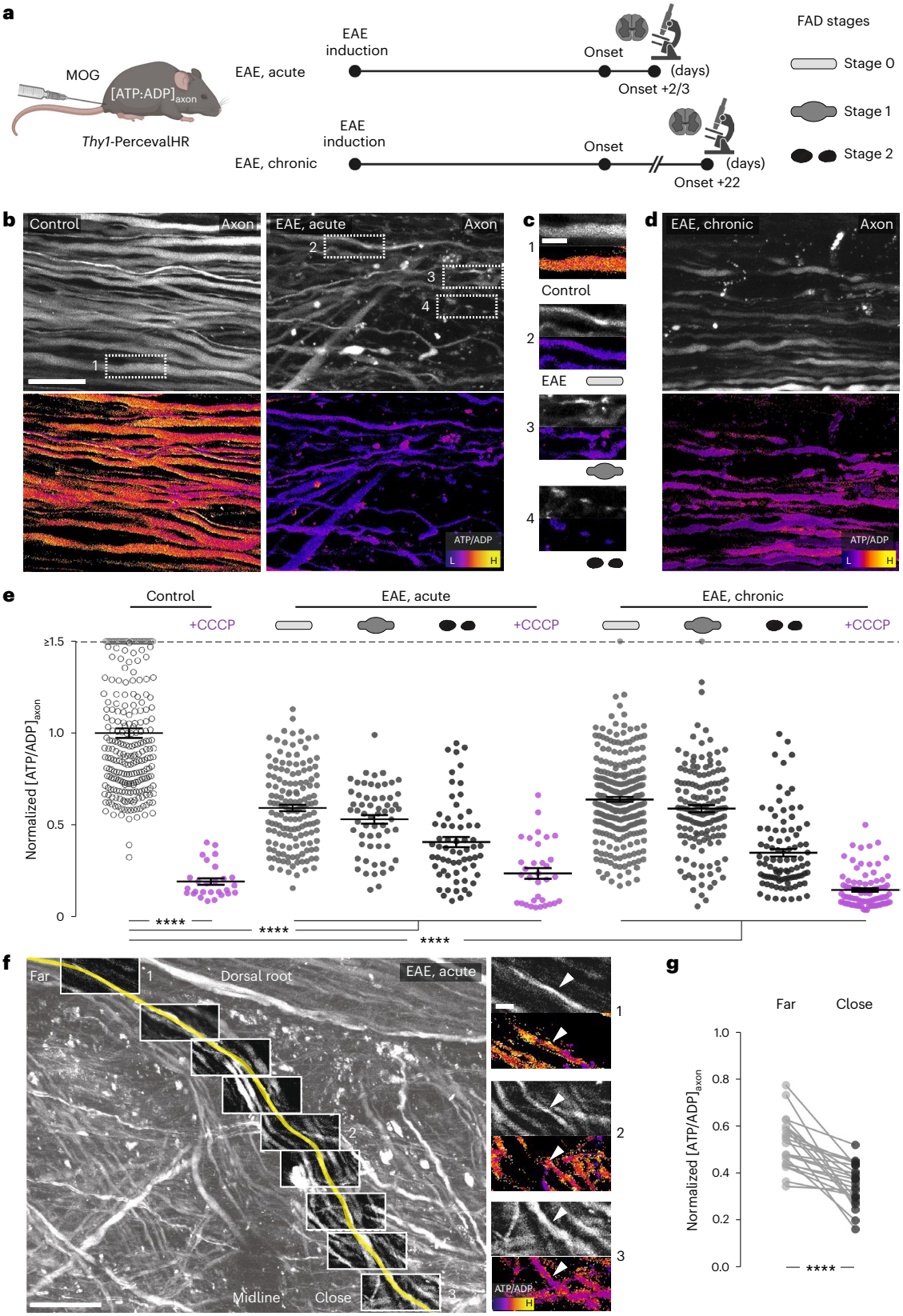

in the spinal cord demonstrated that the sensor can record relevant pathological calcium signals in vivo (Extended Data Fig. 1d–f). We then crossed these reporter mice to *Thy1*-OFP mice to relate axonal morphology to mitochondrial calcium levels and shape in acute EAE lesions. As with our analysis of mitochondrial redox state, we found that mitochondrial calcium levels are primarily increased in fragmented (stage 2) axons, that is, during the end stage of FAD, whereas normal-appearing (stage 0) and swollen (stage 1) axons showed no pronounced calcium dyshomeostasis, despite clear morphological signs of organelle damage (Fig. 2f–j).

Taken together, these experiments indicate that overt dysregulation of the mitochondrial redox state and calcium handling are rather late events during inflammatory axon degeneration. Hence, a molecularly distinct dysregulation of mitochondrial function and molecular composition must explain the prodromal and pervasive ATP deficits in EAE axons.

MitoTag analysis reveals depletion of ETC and TCA cycle components

To obtain an unbiased characterization of the neuroinflammatory changes to the molecular make-up of neuronal mitochondria, we adapted a cell-type-specific proteomics approach that we recently established[23]. For this, we performed intrathecal injections of a rAAV.hSyn:Cre virus into the ventricles of *MitoTag* neonates, which resulted in the tagging of the outer membrane of neuronal mitochondria with green fluorescent protein (GFP). This enabled selective isolation and subsequent mass spectrometry analysis of these mitochondria from the spinal cords of healthy mice, as well as from different stages of EAE (Fig. 3a,b, Extended Data Fig. 3a–c and Supplementary Table 1), which revealed pronounced changes to the mitochondrial proteome of neurons. These changes could not be predicted by protein lifetime, location inside the mitochondria or whether a protein was encoded in the nucleus versus the mitochondrial DNA (Extended Data Fig. 3d–f). Gene set analysis of the major dysregulated pathways converged on the ETC and TCA cycle, which are abundant in healthy neuronal mitochondria, but depleted in acute neuroinflammatory lesions (Fig. 3c,d and Extended Data Fig. 3g,h). The ETC complexes were uniformly affected, typically more strongly in acute than in chronic EAE lesions (Fig. 3d and Extended Data Figs. 3g,h and 4a). This corresponded with reduced axon complex IV (COX) activity as measured in situ by a histochemical assay[24] (Extended Data Fig. 4b,c) and corroborated the previously described neuronal ETC dysfunction in neuroinflammatory lesions[5]. Notably, however, TCA cycle enzymes also showed pronounced dysregulation (Fig. 3d,e). To corroborate these proteomic findings in EAE, expand them to MS and probe their bioenergetic significance, we focused our further analysis on Idh3, which mediates the irreversible oxidative decarboxylation of isocitrate and Mdh2, which oxidizes malate to oxaloacetate. Both enzymes generate NADH, which is subsequently used for ATP generation by the ETC, with Idh3 being rate-limiting for the TCA cycle, while Mdh2 catalyzes a key reaction that links the TCA cycle to anaplerotic reactions[25,26]. At the same time, Idh2, which accelerates the reversible NADP-dependent conversion of isocitrate to α-ketoglutarate, seems to be differentially affected from Idh3 and Mdh2, as its abundance is unchanged in proteomes from acute and increased in chronic neuroinflammatory lesions (Fig. 3d,e). Expression changes of key TCA-cycle-related enzymes, including Idh3, Idh2 and Mdh2, were also present at the transcriptional level as revealed by analysis of published RiboTag translatomes of spinal motoneurons in EAE[27] (Fig. 3f). Hence, neuroinflammation caused a marked alteration in the expression of TCA cycle enzymes, including the rate-limiting enzyme Idh3, which likely hinders neuronal mitochondria from generating sufficient amounts of ATP.

Axonal Idh3 and Mdh2 are depleted in EAE and MS lesions

We next aimed to confirm the proteomics results by immunofluorescence analysis of neuronal mitochondria in EAE, as well as in MS lesions. First, we quantified the expression levels of a subset of TCA cycle enzymes, for which the neuronal *MitoTag* analysis predicted dysregulation in EAE. We performed immunostainings on spinal cord sections from *Thy1*-mitoRFP mice[19], where analysis can be restricted to red fluorescent protein (RFP)-tagged neuronal somata mitochondria. Indeed, the levels of Idh3a (Fig. 4b,d), as well as Mdh2 (Fig. 4e,g) were decreased by more than 50% in EAE lesion-adjacent areas compared to controls. As predicted by our proteomics analysis, the expression of Idh2 was slightly increased (Fig. 4h,j). We further confirmed the depletion of Idh3a and Mdh2 in axons per se, the neuronal compartment where we detected ATP depletion (Fig. 4c,d,f,g). Second, to explore whether similar expression changes of TCA cycle enzymes were also present in MS lesions, we performed immunofluorescence analysis of axonal Idh3a, Idh2 and Mdh2 in brain biopsy and autopsy sections from seven patients with MS (Extended Data Table 1). As fixation protocols are typically variable in patient-derived material, we internally normalized the expression of a given TCA cycle enzyme between the lesion area and the adjacent normal-appearing white matter (NAWM) on the same section (Fig. 5a). This analysis revealed a reduction of Idh3a and Mdh2 in MS lesions (Fig. 5b–e), which was also apparent in chronic active MS lesions, indicating that depletion of TCA cycle enzymes persists long term. Notably, Idh2 expression was not markedly affected, as predicted from the animal model (Fig. 5f,g). Taken together, our findings suggest that TCA cycle disruption is a persistent neuronal change during MS lesion formation and progression.

Idh3a or Mdh2 overexpression ameliorate axonal ATP deficits

Considering the pronounced depletion of Idh3a in EAE and MS, as well as its critical role in the TCA cycle, we explored whether overexpression of individual depleted TCA cycle components, such as Idh3a,

Fig. 2 | Late changes in axonal ROS and calcium homeostasis in EAE lesions. **a**, Experimental design to measure mitochondrial ROS ($[ROS]_{mito}$) in EAE. **b**, Maximum intensity projections of in vivo confocal image stacks of spinal cord axons of control (top) and acute EAE (bottom) in *Thy1*-mitoGrx-roGFP × *Thy1*-OFP mice. Orange fluorescent protein (OFP) channel shown with grayscale LUT (left). Ratiometric LUT of $[ROS]_{mito}$ (λ_{ex} ratio 405 nm/488 nm, indicated as R/R_0) (right). **c**, Details from **b**. Mitochondrial morphologies and $[ROS]_{mito}$ in normal-appearing, swollen and fragmented axons in acute EAE; grayscale LUT of OFP channel above ratiometric $[ROS]_{mito}$ images (top to bottom). **d**, Average $[ROS]_{mito}$ of single axons in control and acute EAE mice normalized to control mean (mean ± s.e.m.; 63 axons from five control mice and 137 axons from six EAE mice compared by one-way analysis of variance (ANOVA) and Tukey's multiple comparison test). **e**, Single-organelle correlation analysis of mitochondrial shape factor (length:width ratio) and $[ROS]_{mito}$ of axons plotted in **d**. Percentages indicate fraction of mitochondria with $[ROS]_{mito}$ > control mean + 3 × s.d. (orange line) in each axon stage. **f**, Experimental design to measure mitochondrial Ca^{2+} levels ($[Ca^{2+}]_{mito}$) in EAE. **g**, Maximum intensity projections of in vivo multiphoton images of spinal cord axons of control (top) and acute EAE (bottom) in *Thy1*-mitoTwitch2b × *Thy1*-OFP mice. OFP channel shown with grayscale LUT (left). Ratiometric LUT of $[Ca^{2+}]_{mito}$ (yellow fluorescent protein (YFP) to cyan fluorescent protein (CFP) emission ratio) (right). **h**, Details from **g**. Mitochondria morphologies and $Ca^{2+}{}_{mito}$ represented as in **c**; grayscale LUT of OFP channel above ratiometric $Ca^{2+}{}_{mito}$ images (top to bottom). **i**, Average $Ca^{2+}{}_{mito}$ of single axons in control and acute EAE mice normalized to mean of controls (mean ± s.e.m.; 138 axons from nine control mice and 192 axons from 11 EAE mice compared by one-way ANOVA and Tukey's multiple comparison test). **j**, Single-organelle correlation analysis of mitochondrial shape factor (length:width ratio) and $[Ca^{2+}]_{mito}$ of axons plotted in **i**. Percentages indicate fraction of mitochondria with $[Ca^{2+}]_{mito}$ > control mean + 3 × s.d. (orange line) in each axon stage. Arrow heads indicate axons with different FAD stages. Scale bars, 25 µm (**b**,**g**) and 10 µm (**c**,**h**). ****$P < 0.001$. See source data for individual data points and further statistical parameters. Illustration created with BioRender.

https://doi.org/10.1038/s42255-023-00838-3

the enzyme's catalytic subunit[28], could restore axonal ATP levels in neuroinflammatory lesions. We initially focused on Idh3 because of its role as a pacemaker enzyme of the TCA cycle[29] and the substantial translational efforts that are underway to target Idh enzymes as these are mutated in several cancers[30–35]. For overexpressing Idh3a together with a fluorescent marker (tdTomato), we used the systemic injection of a rAAV.PHP.eB virus, which drives transgene expression via a pan-neuronal promoter (human synapsin)[36]. Confocal analysis confirmed that a substantial fraction of CNS neurons was transduced with the rAAV.hSyn:Idh3a-tdTomato virus as indicated by tdTomato expression. Moreover, tdTomato-labeled neurons in EAE spinal cords showed a marked increase in mitochondrial Idh3a expression (Extended Data Fig. 5). We then directly assessed the effects of Idh3a restoration on axonal energy deficits in neuroinflammatory lesions by

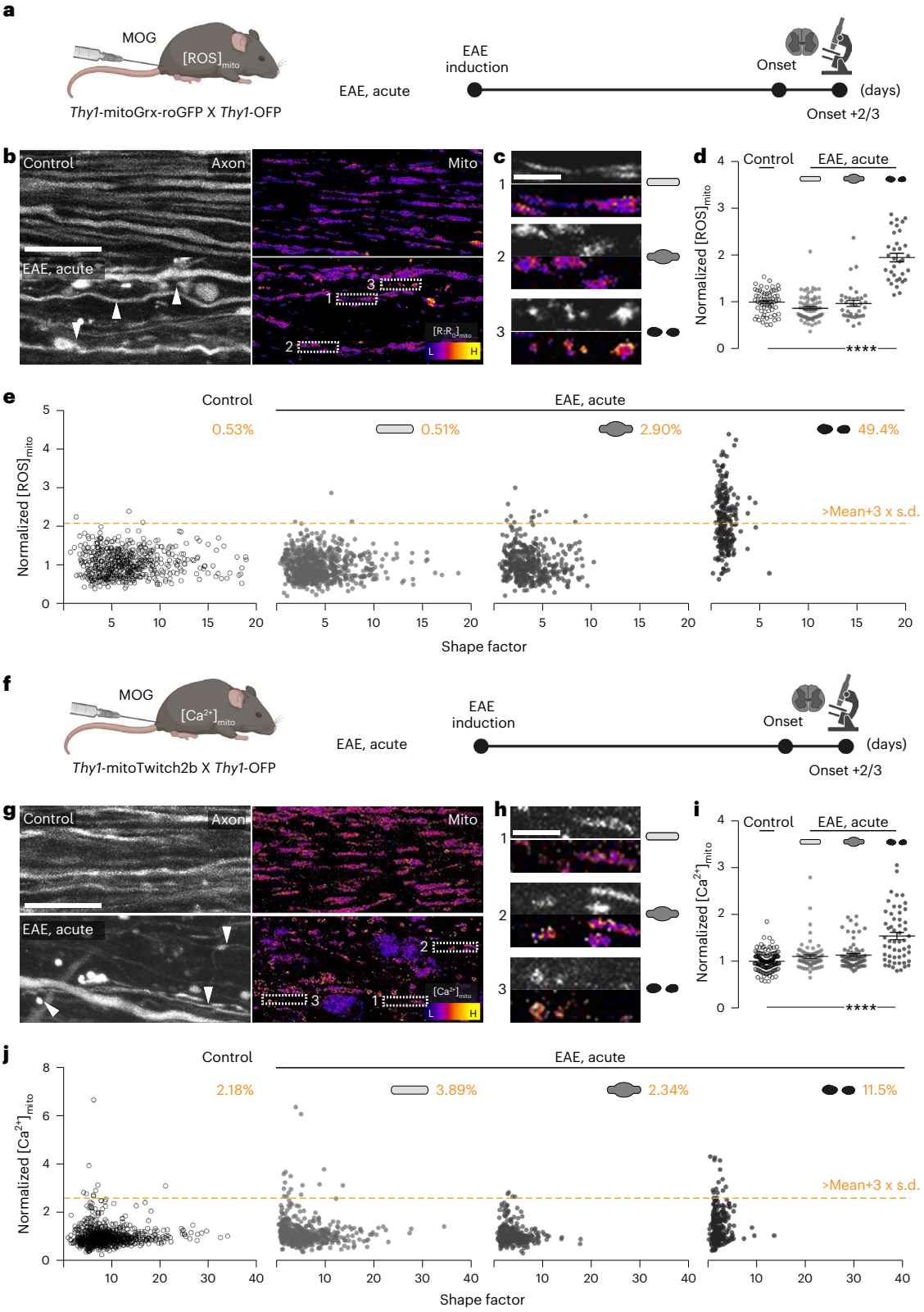

https://doi.org/10.1038/s42255-023-00838-3

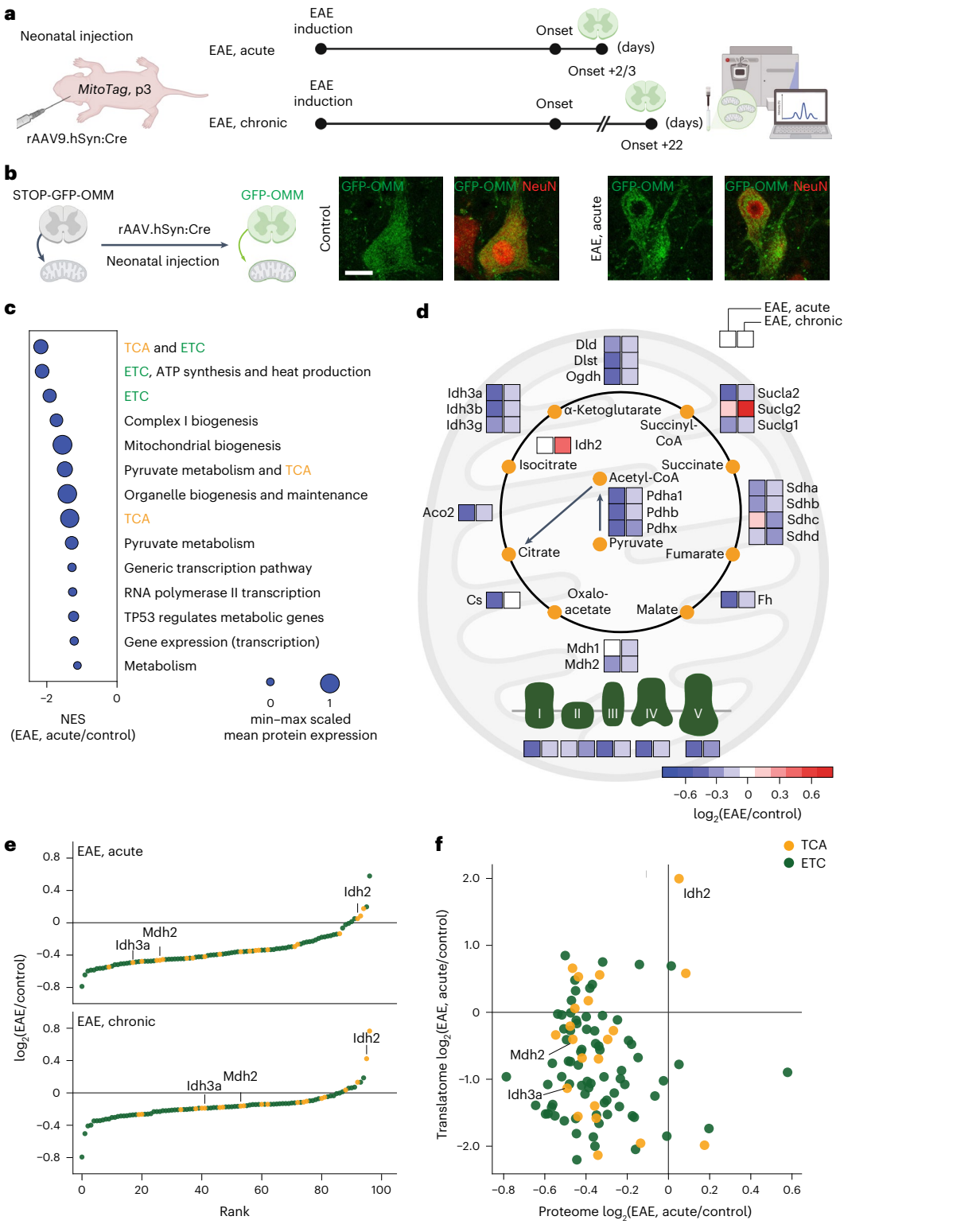

Fig. 3 | ETC depletion and TCA cycle imbalance in neurons during EAE. **a**, Experimental design for combined AAV/*MitoTag*-based proteomic analysis of neuronal mitochondria in EAE. **b**, Confocal image of GFP expression (green) in rAAV9.hSyn:Cre transduced neurons (NeuN; red) in a control and EAE *MitoTag* mouse spinal cord. **c**, Annotations of the most downregulated pathways (Reactome[59,60], v.7.4) in *MitoTag* proteomes of neuronal mitochondria in acute EAE. Dot size indicates min–max scaled mean protein expression level ranged from 0 to 1. NES, normalized enrichment score. **d**, Relative abundance of the TCA cycle and ETC components in neuronal mitochondria. Average shown as color-coded $\log_2$(EAE/control) for acute and chronic EAE compared to respective controls. **e**, Rank of TCA cycle (orange) and ETC (green) proteins according to $\log_2$FC expression in acute (top) and chronic (bottom) EAE. **f**, Correlation between neuronal transcript and protein levels of TCA cycle and ETC proteins in EAE. Translatomic data were re-analyzed from Schattling et al.[27]. The acute cohort was collected from six control and five EAE acute mice and the chronic cohort was collected from five control and five EAE chronic mice. Scale bars, 25 µm in **b**. See source data for individual data points and further statistical parameters. See source data for individual data points and further statistical parameters. Illustration created with BioRender.

inducing EAE in *Thy1*-PercevalHR mice injected with either the rAAV.hSyn:Idh3a-tdTomato virus or a control rAAV.hSyn:Cre-tdTomato virus, carrying a similarly sized, but in our setting inert transgene. In vivo imaging of the surgically exposed spinal cord in EAE-induced animals again confirmed strong tdTomato expression in a fraction of axons, while other PercevalHR-expressing axons were tdTomato-negative and provided an internal control (Fig. 6a,b). Compared to this control axon population (which rules out general effects on lesion activity by the virus), transduction with a rAAV.Syn:Idh3a-tdTomato virus significantly increased the ATP/ADP ratio and thus partially restored the axonal energy deficiency in neuroinflammatory lesions (Fig. 6c). No such rescue was observed in axons transduced with the control rAAV.hSyn:Cre-tdTomato (Fig. 6d). Notably, ATP/ADP ratios rose in axons of all damage stages, suggesting that correcting Idh3a levels could also counteract ATP deficiencies in more advanced stages of FAD. By extending the observation period from the acute phase after the EAE peak by 3 weeks, we confirmed that both the reduction in ATP/ADP ratio and a reversing effect of Idh3a overexpression persisted, albeit the latter's effects seemed to abate (Extended Data Fig. 6a–c). Next, we asked whether the effect of overexpressing Idh3a would be unique to this enzyme by targeting Mdh2 in a similar way. We observed that also viral gene transfer of Mdh2 partially restored axonal ATP/ADP levels in neuroinflammatory lesions, at least in advanced stages of axon damage (Extended Data Fig. 7).

Overall, these results suggest that a combinatorial targeting of the TCA cycle, or rather a metabolic approach to boosting TCA cycle function, will be needed to more optimally remedy axonal bioenergetics in neuroinflammation; indeed, when we explored the effects of Idh3a overexpression on axonal morphologies in tdTomato-positive versus tdTomato-negative axons, we could not detect robust differences in axonal swelling or fragmentation at 3 weeks after disease onset (Extended Data Fig. 6d).

Discussion

That axons in neuroinflammatory lesions exist in a state of 'energy failure' linked to mitochondrial damage has long been inferred based on (1) abnormalities in mitochondrial density, dynamics and morphology; (2) mitochondrial dysfunction as revealed by in situ assays of respiratory complex function or mitochondrial potential; and (3) the accumulation of mitochondrial DNA mutations in inflamed CNS tissue[1,2,18]. Furthermore, there is molecular evidence that axons in MS lesions might exist in a hypoxic state, which would further restrict mitochondrial respiration[37]. These data have directed most attention to the ETC, which covers most of the uniquely high energy demands of neurons and determines the mitochondrial potential and other aspects of respiration that can be assayed in situ, for example, using enzymatic assays. Thus, the focus on the ETC is both well justified by its importance, but also biased by experimental accessibility. At the same time, the ETC is not necessarily a good therapeutic target, given its complex molecular make-up at the protein, as well as at the genome level, the extremely low turnover of some of its components and its Janus-faced nature as the major source not only of ATP, but also of oxygen radicals. Finally, the ETC needs to be fed with a steady and sufficient flow of redox equivalents and other substrates, most of which derive from the TCA cycle. Hence the TCA cycle, as the 'upstream' bioenergetic hub of metabolism, also deserves attention in the context of the presumed 'energy failure' of axons in neuroinflammation[38]. Especially so, as the TCA cycle is increasingly emerging as a metabolic hub relevant to neurodegeneration[25] and a 'druggable' target, for example in cancer[31,39].

Against this backdrop, the present study makes the following contributions: (1) We demonstrate directly by in vivo biosensor measurements (both using PercevalHR to measure the ATP/ADP ratio, as well as ATeam, which assays ATP levels) that most axons in neuroinflammatory lesion exist in a state of depressed cytoplasmic ATP availability, already during early stages of the axonal degeneration pathway. Moreover, this change precedes overt signs of mitochondrial redox or calcium dyshomeostasis. (2) We show by molecular profiling of neuronal mitochondria not only a disruption of the ETC, but a similarly profound alteration of the 'upstream' TCA cycle, where a number of enzymes, including Idh3 and Mdh2, are depleted in neuronal mitochondria in EAE and MS lesions. (3) Finally, we demonstrate that overexpressing Idh3a (the catalytic subunit of the enzyme) or Mdh2 suffices to increase axonal ATP provision, albeit to a limited extent. This suggests, on the one hand that the axonal energy crisis caused by neuroinflammation is due to a dual deficiency, both of redox substrate provision from the TCA cycle to the ETC, as well of oxidative phosphorylation itself. On the other hand, a full rectification of these neuroenergetic deficits will likely require a manipulation of either a master regulator or multiple enzyme targets in parallel.

Together, the results we present here expand our understanding of the molecular pathogenesis of immune-mediated mitochondrial damage and propose new avenues for therapeutic intervention. They also raise the question of where the dysregulation of the TCA cycle originates. Overall, the pattern of mitochondrial proteome changes does not relate to any simple pattern that we could discern. While the overall mitochondrial mass in neurons cannot be estimated easily by this method, the data suggest that within the mitochondrial proteome of neurons, specific dysregulation happens, as for example some biosynthetic pathways (such as mitochondrial translation) are upregulated, while most TCA cycle and ETC components are suppressed. Indeed, the parallel and progressive upregulation of Idh2, while Idh3 is downregulated, suggests a specific metabolic 'rewiring' response[40], rather than just a global loss of mitochondrial biogenesis or increase in mitophagy. Most likely, this response involves biosynthetic, as well as proteostatic mechanisms, as the observed dysregulation of mitochondrial proteins does neither correspond to whether a protein is encoded in the mitochondrial DNA (where mutations are known to accumulate in MS)[2,8] versus in the nucleus, nor with the estimated lifetime[41]. Indeed, the correlation of published neuronal translatome data from a similar model[27] with our neuronal proteomes provides direct support for an element of 'anterograde regulation' from the nucleus, while the long lifetimes of some downregulated enzymes (including subunits of Idh3 (ref. 42)) argue for a parallel degradation, given the swift development of the proteomic phenotype in our acute EAE model (which is present in acute lesions 2 d after disease onset).

Fig. 4 | TCA cycle enzymes, Idh3, Idh2 and Mdh2, are dysregulated in neurons in EAE. a, Experimental design to validate dysregulated TCA cycle enzymes identified by *MitoTag* proteomics in EAE. **b**–**j**, Immunofluorescence analysis of Idh3a (**b**–**d**), Mdh2 (**e**–**g**) and Idh2 (**h**–**j**) in spinal cord neuronal somata (top) and axons (bottom) of control (left) or of acute EAE (right) *Thy1*-mitoRFP mice (TCA cycle enzymes, green; RFP, red for neuronal mitochondria in somata or neurofilament (NF) for axonal staining, respectively). Graphs (**d**,**g**,**j**) show area occupancy (soma, $P = 0.5009$ for Idh3a, 0.1371 for Mdh2 and 0.9907 for Idh2; axon, $P = 0.053$ for Idh3a, 0.0357 for Mdh2 and 0.5615 for Idh2), mean fluorescence intensities (MFIs) (soma, $P = 0.0007$ for Idh3a, 0.0003 for Mdh2 and 0.0317 for Idh2; axon, $P = 0.00006$ for Idh3a, 0.0357 for Mdh2 and 0.0299 for Idh2) and their product, integrated density (soma, $P = 0.0046$ for Idh3a, 0.0286 for Mdh2 and 0.265 for Idh2; axon, $P = 0.0079$ for Idh3a, 0.0023 for Mdh2 and 0.0653 for Idh2), in EAE neuronal somata and axons normalized to the mean of control (mean ± s.e.m.; compared per animal by two-tailed, unpaired Student's *t*-test or Mann–Whitney *U*-test where normal distribution could not be confirmed from four control and four EAE mice for Idh3a and Mdh2; five control and five EAE mice for Idh2. Scale bar, 25 µm (**h**) applies also to **b**,**e** and their details; 10 µm (**i**), applies also to **c** and **f**. $^{*}P < 0.05$; $^{**}P < 0.01$, $^{***}P < 0.005$; $^{****}P < 0.001$; NS, not significant. See source data for individual data points and further statistical parameters. Illustration created with BioRender.

https://doi.org/10.1038/s42255-023-00838-3

Irrespective of the origin of the reduced ATP availability that our biosensor measurements reveal, the further question arises of what this implies for axonal survival and hence, given the central role of axon degeneration in MS disease course[43], for possible lasting functional consequences. While limited ATP availability is often cited as a sufficient argument to assume axonal demise and profound and lasting ATP deficiency can clearly cause axon degeneration[44], our observations rather argue for a chronic 'dystrophy' than for an acute bioenergetic

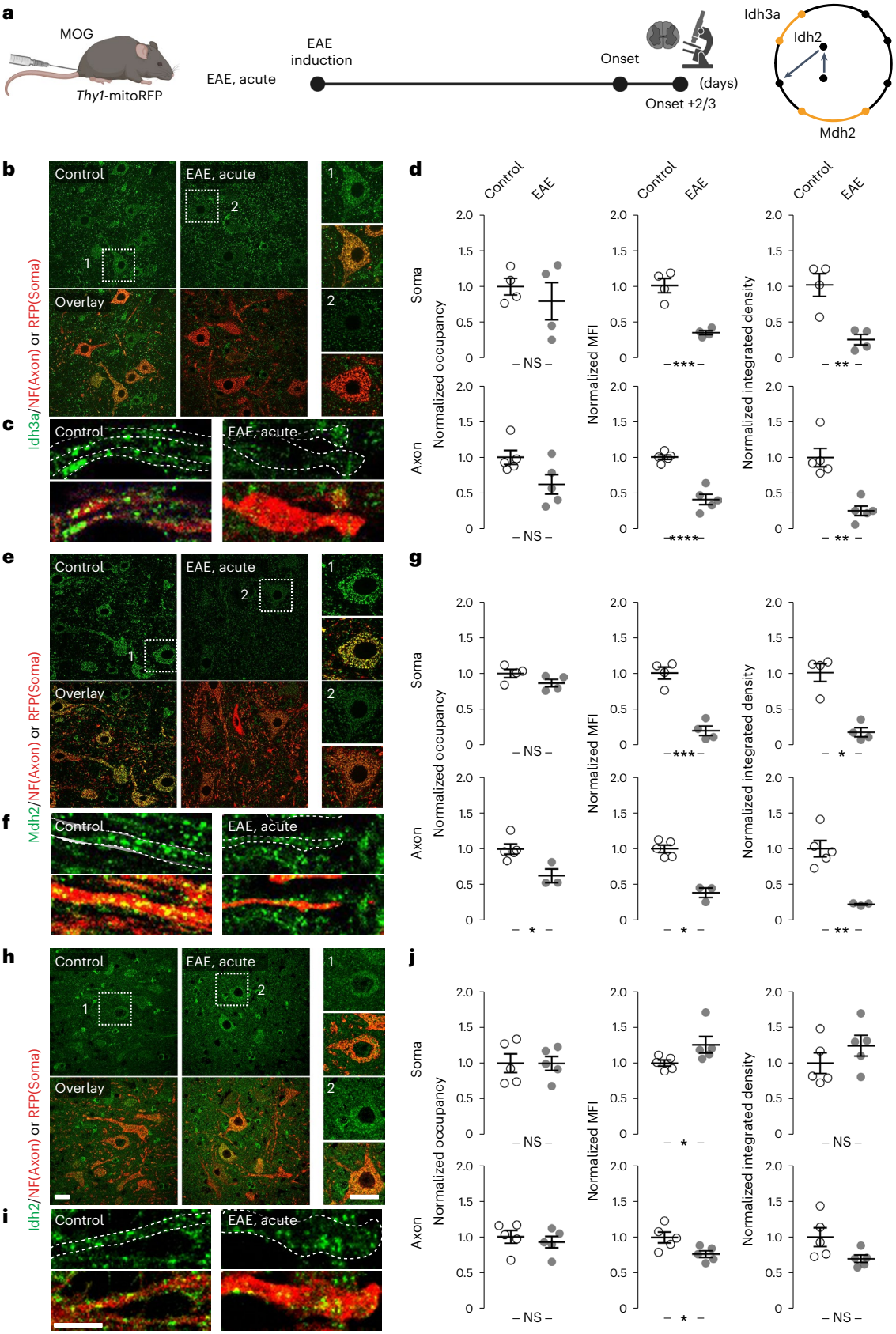

https://doi.org/10.1038/s42255-023-00838-3

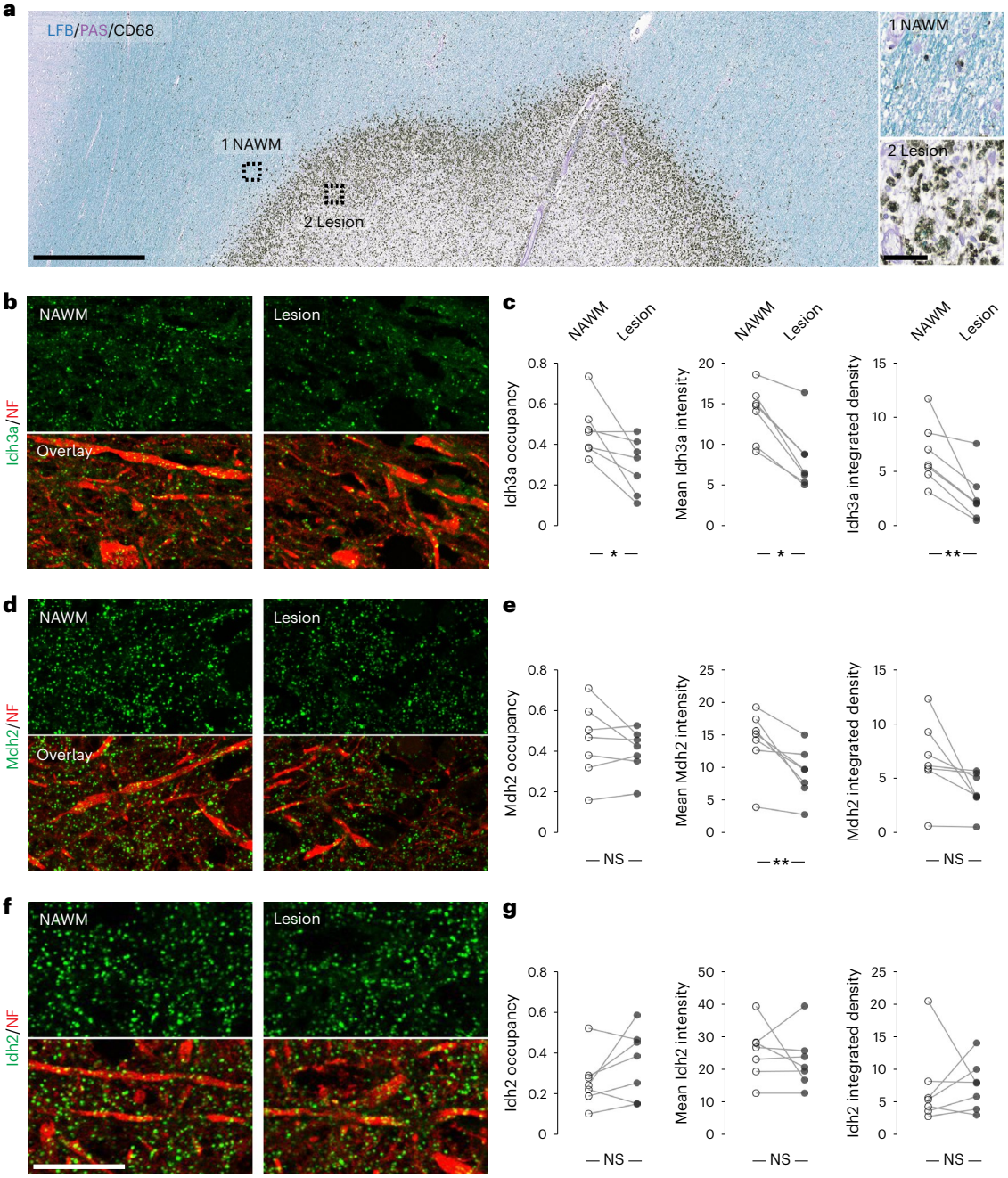

Fig. 5 | TCA cycle enzymes, Idh3, Idh2 and Mdh2, are dysregulated in neurons in MS. a, Overview of an MS lesion in human cortex, with areas of NAWM and the lesion site marked and magnified in insets. Myelin (Luxol fast blue, LFB, blue; periodic acid–Schiff, PAS, purple) and macrophages (CD68, black) are labeled. **b**,**c**, Immunofluorescence analysis of Idh3a in cortical axons in NAWM (left) or lesion areas (right; Idh3a, green; NF, red). **d**,**e**, Immunofluorescence analysis of Mdh2 in cortical axons in NAWM (left) or lesion areas (right; Mdh2, green; NF, red). **f**,**g**, Immunofluorescence analysis of Idh2 in cortical axons in NAWM (left) or lesion areas (right; Idh2, green; NF, red). Graphs (**c**,**e**,**g** show area occupancy ($P = 0.0251$ for Idh3a, 0.2995 for Mdh2 and 0.1599 for Idh2), MFIs ($P = 0.0156$ for Idh3a, 0.0099 for Mdh2 and 0.5144 for Idh2) and their product, integrated density ($P = 0.0075$ for Idh3a, 0.0606 for Mdh2 and 0.6875 for Idh2), in pairs of NAWM and lesion areas from seven cases, as listed in Extended Data Table 1 and compared by two-tailed, paired *t*-test or Wilcoxon matched-pairs signed-rank test where normal distribution could not be confirmed. Scale bars, 1,000 µm (**a**); 50 µm in inset; 25 µm (**f**), also applies to **b** and **d**. $^*P < 0.05$; $^{**}P < 0.01$; NS, not significant. See source data for individual data points and further statistical parameters.

collapse of axons in neuroinflammation. Indeed, we find reduced ATP/ADP ratios, ATP levels and TCA cycle enzyme expression in the majority of axons, even those with a normal morphology. From previous work, we know that only a subset of these axons is at immediate risk of degeneration and some even recover morphological and mitochondrial integrity[6]. Notably, a similarly pervasive pattern of dysfunction has been apparent in our previous studies of axonal transport[17]. As axonal transport is highly ATP dependent and in converse, mitochondria are a major axonal transport cargo[4], a vicious cycle could result in the long-term breakdown of the ATP supply chain, which might not cause immediate axon degeneration, but rather subacute dysfunction. Furthermore, previous reports of in situ ATP measurements in mouse white matter tracts have shown that neuronal activity puts an immediate strain on energy supply[45], which could sensitize specific activity-related

https://doi.org/10.1038/s42255-023-00838-3

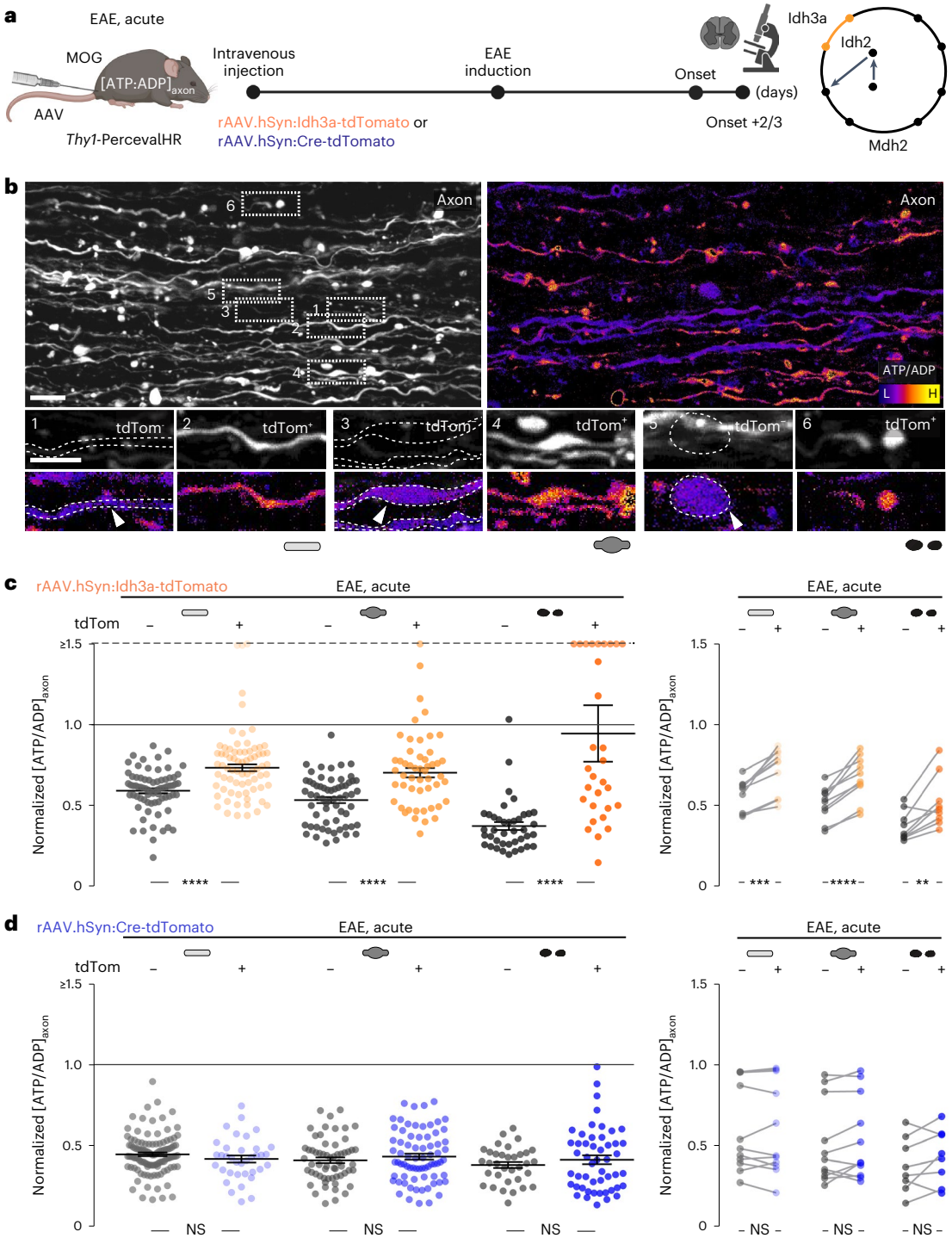

Fig. 6 | Idh3 overexpression ameliorates axonal ATP deficits in EAE lesions. **a**, Experimental design to measure $[ATP/ADP]_{axon}$ in acute EAE in *Thy1*-PercevalHR mice that virally overexpressed Idh3a or a control protein (Cre recombinase) together with tdTomato in a subset of axons. **b**, Maximum intensity projections of in vivo multi-photon image stacks of spinal cord axons in Idh3a-overexpressing *Thy1*-PercevalHR mice. Grayscale LUT of tdTomato (left). Ratiometric $[ATP/ADP]_{axon}$ LUT (λ_{ex} ratio 950 nm/840 nm) (right). Details below show image pairs of tdTomato-negative ($tdTom^-$, left) and tdTomato-positive ($tdTom^+$, right) normal-appearing, swollen and fragmented axons ($tdTom^-$ has dashed outlines) in acute EAE. **c**, Comparison of $[ATP/ADP]_{axon}$ in $tdTom^+$ and $tdTom^-$ axons (plotted as λ_{ex} ratio 950 nm/840 nm, normalized to control axon mean indicated as the black line; values above 1.5 are lined up on the '≥1.5' dashed line). $[ATP/ADP]_{axon}$ of single $tdTom^-$ (gray) and $tdTom^+$ (orange) axons in Idh3a-overexpressing EAE mice (left). Lesion-specific paired analysis of mean $[ATP/ADP]_{axon}$ in $tdTom^-$ (gray) and $tdTom^+$ (orange) axon populations of the three morphological stages (right). **d**, Same analysis as **c**, but in a mouse cohort overexpressing a control protein (Cre recombinase). Mean ± s.e.m. Comparison of 176 $tdTom^-$ axons versus 153 $tdTom^+$ axons in 12 lesions from four mice in **c**; 214 $tdTom^-$ axons versus 159 $tdTom^+$ axons in 11 lesions from three mice in **d** using a two-tailed, unpaired Student's *t*-test (**c**,**d**, left graphs) and a paired *t*-test (**c**,**d**, right graphs). Scale bar, 25 µm (**b**). $^{**}P < 0.01$; $^{***}P < 0.005$; $^{****}P < 0.001$. See source data for individual data points and further statistical parameters. Illustration created with BioRender.

patterns of degeneration. To explore this notion, but also to better understand the relative importance and metabolic consequences of the two aspects of the axonal energy deficiency emerging from the dual dysregulation of the ETC and the TCA cycle, we also performed metabolic modeling[46] (Methods provides details) based on our analysis of mitochondrial proteomes from control and EAE spinal cords. The modeling predicted a diminished absolute availability of ATP, as well as a reduced ATP/ADP ratio, and also suggested that indeed, with growing 'metabolic load' (an increased ATP consumption rate, which in neurons could for example, relate to increased rates of action potential firing and neurotransmission), these deficits should progress (Extended Data Fig. 8a). Furthermore, in silico rectification of groups of proteins to their control levels revealed that while 'normalizing' the ETC had some effect on ATP levels, the TCA cycle enzymes are predicted to be the more efficacious target (Extended Data Fig. 8b).

So how to counterbalance the axonal energy deficiency? Indeed, 'brain energy rescue' has been hailed as a possible therapeutic strategy across neurological disorders[47]. The most direct approach would be the provision of energy substrates or key cofactors for the function of bioenergetic enzymes. Indeed, first trials along these lines, for example providing biotin, have been conducted in MS, but failed[48]. Notably, biotin is required for the activity of enzymes that feed into the TCA cycle upstream of Idh3 and Mdh2. Our data on TCA cycle disruptions, combined with the previous insights on ETC dysfunction, would argue that simply feeding a substrate or co-factor into a broken supply chain will indeed not be efficient. Therefore, key bottlenecks in the ATP-providing metabolic pathways need to be unblocked in addition. Our data show, in accordance with our modeling predictions, that while addressing single bottlenecks, such as Idh3 (a key 'pacemaker' enzyme of the TCA cycle[29]) might have some benefits, such a focused intervention would only result in limited changes to the neuronal energy state. While the fact that Idh3 activity can be directly allosterically stimulated by a low ATP/ADP ratio[49] and activated by calcium[50], two changes that are induced in axons in response to an inflammatory challenge, argue that Idh3a overexpression might have a comparably strong unblocking effect on the TCA cycle, our results with Mdh2 overexpression show that multiple target points exist within this pathway upstream of the ETC. For actual benefits on axonal survival and neurological deficits, we assume that a combinatorial intervention will be needed; in accordance with our observation that even if we extended Idh3 overexpression for several weeks after EAE onset, no clear reduction in axon pathology was apparent. Moreover, we expect the effects of neuroenergetic dystrophy to really only manifest in the slow-evolving late states of chronic neuroinflammation that likely drive progression in MS. Unfortunately, animal models of this key phase of MS largely remain elusive. Thus, while the data presented here provide proof of the principle for TCA cycle targeting, they probably do not yet foreshadow a true translational strategy.

Still, the fact that the TCA cycle enzymes are the focus of substantial biomedical interest[51,52], given the key role of some of them (such as Idh1 and Idh2, but also Mdh2) in cancer biology, suggests that multi-pronged targeting of TCA-cycle-related pathways in neuroinflammation might be a viable translational development. Notably, Idh3 seems to be dysregulated in some neoplasms, including glioblastomas[53]. This has resulted in the development of Idh targeting drugs, for example for certain leukemia and brain tumor subtypes[52,53]. In cancer, the detrimental consequence of Idh mutations seems to be metabolic rerouting that enhances tumor cell proliferation and immune cell dysregulation[34]. Indeed, also in neuroinflammation some aspects of axonal dysfunction resulting from TCA cycle disruptions could be due to metabolite imbalances rather than mere lack of efficient fueling of the ETC and hence ATP deficiency. In this context, the concomitant upregulation of Idh2 in chronic stages of our model is notable and raises important questions for future exploration, for example by metabolomic analysis of cell-type-specific mitochondria. Such analysis could be combined with pharmacological intervention, to reroute substrates into the diminished bioenergetic pathways of axons in an inflammatory milieu. For instance, could the available Idh blockers, most of which are deliberately not targeting Idh3, still be useful in forcing metabolic flow back into the TCA cycle? Similarly, could approaches of increasing mitochondrial mass (such as overexpression of PGC1α, which is beneficial in inflammatory demyelination and regulates Idh3a expression as part of its broad transcriptional effects[11,52]) be synergistic with targeting the TCA cycle to unblock energy provision in axons and resolve their dystrophy in conditions like MS? The identification of the TCA cycle and some of its key enzymes as a disease contributor and a potential therapy target indeed opens the possibility for such a comprehensive evaluation of strategies to mitigate the neuronal energy crisis in the inflamed CNS.

Methods

Animals

All experiments were performed on either postnatal day 3 pups or adult mice according to the protocols on a C57BL/6 (strain designation C57BL/6J, Jackson Laboratories) background at age 2–6 months. All animals were bred and housed under standard conditions with a 12-h light–dark cycle at a temperature of 22 ± 2 °C and 55 ± 10% relative humidity. Food and water for mice were provided ad libitum. Female and male were equally allocated into control and experimental groups if not explicitly mentioned otherwise. The experiments were not powered for independent analysis of male and female mice, but separate analysis of female and male mice did not reveal any major sex-specific effects in our analyses of ATP/ADP levels. All experimental procedures were conducted in accordance with regulations of the relevant animal welfare acts and protocols approved by the responsible regulatory office.

To measure neuronal mitochondrial redox changes in spinal axons, we used the *Thy1*-mitoGrx-roGFP mouse line, which selectively expresses the redox sensor Grx-roGFP2 in neuronal mitochondria[19]. To visualize axonal morphology, these mice were crossed to *Thy1*-OFP mice[20], in which neurons are labeled by cytoplasmic expression of an OFP. To investigate the proteomic profile of neuronal mitochondria in the context of neuroinflammation, we used the *Gt(ROSA)26Sor MitoTag* knock-in mouse line generated by recombinase-mediated cassette (*loxP*-flanked STOP) exchange into the Rosa26 locus that allows a Cre-dependent expression of GFP targeted to the outer mitochondrial membrane. The *MitoTag* mouse line is available from The Jackson Laboratory as JAX#032675 (Rosa26-CAG-LSL-GFP-OMM)[23]. *Thy1*-mitoRFP mice, in which tagRFP is localized to the matrix of neuronal mitochondria[19] were used to ascertain the localization of immunofluorescence signals to neuronal mitochondria.

Generation of reporter mouse lines

To measure the neuronal ATP/ADP ratio, a *Thy1*-PercevalHR mouse lines were generated using a blunt-end cloning strategy with Perceval GW1-HR plasmid (Addgene, #49082) purchased from Addgene[13]. In brief, the GW1-Perceval-HR plasmid was digested with Xba1 and EcoRI enzymes, blunted and inserted into the *Thy1*-vector cut beforehand with XhoI, blunted and dephosphorylated. After ligation and electroporation, minipreps of ampicillin-selected *Escherichia coli* cultures were performed, followed by verifying the correct plasmid orientation and enzyme digestions. The construct was transfected in human embryonic kidney 293T (HEK) cells and cytoplasmic expression was confirmed by confocal microscopy. Maxipreps of the adequate cloning candidates were carried out using QIAGEN kits. The Thy1-Perceval-HR plasmid was further linearized using PvuI and EcoRI restrictions enzymes.

To measure the calcium level in neuronal mitochondria, *Thy1*-mitoTwitch2b mouse lines were generated. The Twitch2b-pcDNA3 plasmid[22] was kindly provided by O. Griesbeck (Max Planck Institute of Neurobiology). The Twitch2b sensor was extracted using NotI restriction enzyme and inserted into the pCMV:myc-mito plasmid (Addgene, #71542) cut beforehand with NotI restriction enzyme and

dephosphorylated. After ligation and electroporation, minipreps of ampicillin-selected *E. coli* cultures were performed, followed by verifying the correct plasmid orientation and correct enzyme digestions. The construct was transfected in HEK cells and verified by live imaging. After retesting the construct and its functional responsiveness in HEK cell culture, maxipreps of the adequate cloning candidates were carried out using QIAGEN kits. The pCMV-myc-mito-Twitch2b sequence was further extracted using PmI and XbaI, blunted and inserted into the *Thy1*-vector cut beforehand with XhoI, blunted and dephosphorylated. The *Thy1*-mitoTwitch2b plasmid was linearized using ZraI and AflIII restrictions enzymes. Sequencing of *Thy1*-mitoTwitch2b and *Thy1*-PercevalHR constructs was performed by Eurofins. The sample purity of the linearized DNA was determined using the absorbance ratio at 260 nm versus 280 nm. The concentration of the linearized DNA used for pronuclear injections was 45.2 ng μl^{-1} in 60 µl for Thy1-Perceval-HR (with a ratio A260:280 of 1.83) and 36.5 ng μl^{-1} in 120 µl (with a ratio A260:280 of 1.83) for *Thy1*-mitoTwitch2b. The generation of the *Thy1*-PercevalHR and *Thy1*-mito-Twitch2b was conducted at the Transgenic Core Facility of the Max Planck Institute for Molecular Cell Biology and Genetics in Dresden by standard pronuclear injections into pseudo-pregnant host mice. For analysis of mitochondrial calcium level in spinal axons *Thy1*-mitoTwitch2b mice were crossed to *Thy1*-OFP mice.

AAV vector generation and virus production

The AAV.hSyn:Cre plasmid, which encodes for Cre recombinase expression specifically in neuronal populations under the control of the human synapsin promoter, was generated by replacing the DIO-GFP sequence (Addgene, #50457) to create the AAV.hSyn backbone plasmid. In brief, the AAV.hSyn:DIO-GFP plasmid was initially digested with SalI/XhoI, followed by incubating with BglII to remove DIO.GFP and ligated with GFP.ires.Cre, which had been excised from AAV.CMV:GFP.ires.Cre with BglII, using Quick Ligase according to the manufacturer's instruction. Further from AAV.hSyn:GFP.ires.Cre, GFP.ires was excised with BmgBI and the backbone was ligated to acquire the AAV.hSyn:Cre plasmid.

The AAV.hSyn:Idh3a.P2A.tdTomato plasmid, which enables Idh3a.P2A.tdTomato expression under the control of the human synapsin promotor was generated as follows. The AAV.hSyn:DIO.FGF.P2A.EGFP was initially digested with SalI/HindIII to remove DIO.FGF.P2A.EGFP, ligated with an amplified Idh3a fragment (Sino Biological, MG53630-UT; forward primer: gtaccggatcctctagaggccgccaccaagc and reverse primer: gcttccgtctaagtctttgactctacgacagatttcttctg) and an amplified P2A.tdTomato sequence (forward primer: aaagacttagacggaagcggagccac and reverse primer: tccagaggttgattatcgatacgttacttatacagctcatcca) by using Gibson assembly master mix (New England Biolabs, E2611S). The AAV.hSyn:mMDH2.P2A.tdTomato plasmid, which encodes for Mdh2.P2A.tdTomato expression under the control of the human synapsin promotor was generated as follows. The AAV.hSyn:DIO.FGF.P2A.EGFP was initially digested with SalI/HindIII to remove DIO.FGF.P2A.EGFP, ligated with an amplified Mdh2 fragment (Sino Biological, MG51925-UT; forward primer: gtaccggatcctctagaggccgccaccaagc and reverse primer: ccgcttccctcatgttcttgacaaagtcctcgcct) and an amplified P2A.tdTomato sequence (CAG.Cre.P2A.tdTomato; forward primer: catgaagggaagcggagccactaacttc and reverse primer tccagaggttgattatcgatacgttacttatacagctcatcca), by using Gibson assembly master mix.

The AAV.hSyn:ATeam plasmid, which encodes for ATeam, a FRET-based ATP indicator, under the control of the human synapsin promoter was generated as follows. AAV.hSyn:DIO.FGF.P2A.EGFP was initially digested with SalI/HindIII to remove DIO.FGF.P2A.EGFP, ligated with amplified ATeam fragment (Addgene, #51958; forward primer: tccagaggttgattatcgataatagggccctctagatgcatgctc and reverse primer: gtaccggatcctctagaggagacccaagcttggtaccg) by using Gibson assembly master mix.

The AAV.hSyn:SypHer3s plasmid, which encodes for SypHer3s, a ratiometric pH probe, under the control of the human synapsin promoter was generated as follows. AAV.hSyn:DIO.FGF.P2A.EGFP was initially digested with SalI/HindIII to remove DIO.FGF.P2A.EGFP, ligated with an amplified SypHer3s fragment (Addgene, #108118; forward primer: gtaccggatcctctagaggccgccaccatgtccggacc and reverse primer: tccagaggttgattatcgataccgtcgactgcagaattctca) by using Gibson assembly master mix.

The AAV.hSyn:Cre.P2A.tdTomato plasmid used to express Cre and RFP dTomato specifically in neurons was purchased from Addgene (Addgene, #107738). The construct with the correctly oriented insert was introduced to Stellar Competent cells (Clontech, 636763) and the plasmid purification was performed with a QIAGEN Plasmid Maxi kit according to the manufacturer's protocol.

AAV vector packaging was performed using HEK 293T (ATCC, crl-3216) and produced as described. HEK 293T cells were transfected with pAD-helper, AAV-capsid 9 (Addgene, #112865) or PHP.eB[36] (Addgene, #103005) and the AAV-construct (molar ratio 1:1:1) using an RPMI: PEI incubation protocol. AAV vectors were collected from the supernatant with polyethylene glycol (Sigma-Aldrich, no. 25322-68-3) solution and the cell pellets. Freeze–thaw cycles were performed to lyse the cells and the residual DNA from the packaging was further degraded with benzonase (Sigma-Aldrich, E1014). Following the purification procedure using iodixanol gradient ultracentrifugation, the virus was concentrated by subsequent centrifugation and incubation with formulation buffer (Pluronic-F68 0.001% in saline PBS). The product was then further collected (with a genomic titer of ~10^{12} to 10^{14}) and stored in small aliquots at −80 °C.

Neonatal intraventricular injection of rAAV

For the proteomic profiling of mitochondria in neuroinflammation, AAV.hSyn:Cre was injected into neonatal *MitoTag* pups (genotype, WT/MitoTag) according to a previously published protocol[54]. In short, P3 pups were anesthetized with isoflurane (Abbott) and injected with 3 µl (~1×10^{12} viral particles per animal) AAV9.hSyn:Cre with 0.05% (wt/vol) trypan blue to the right lateral ventricle at a rate of 30 nl s^{-1} using a fine glass pipette (Drummond; 3.5″, 3-000-203-G/X) attached to a nanoliter injector (World Precision Instruments; Micro4 MicroSyringe Pump Controller connected with Nanoliter 2000) held by the stereotaxic manipulator. All surgeries were conducted under ultrasound guidance (VisualSonics; Vevo1100 Imaging System, with a Microscan MS550D transducer).

Intravenous injection of rAAV

To achieve overexpression of TCA cycle proteins or biosensors in spinal axons, AAV.PHP.eB.hSyn:Idh3a.P2A.tdTomato, AAV.PHP.eB.hSyn:Mdh2.P2A.tdTomato, AAV.PHP.eB.hSyn:ATeam, AAV.PHP.eB.hSyn:Cre.P2A.tdTomato or AAV.PHP.eB.hSyn:SypHer3s was intravenously injected 14 d before EAE induction. For this, the animal was immobilized and the tail was locally warmed to dilate the vessels facilitating the injection. The mice were injected with the virus (~1×10^{11} viral particles per animal) at a final volume of 120 µl, followed by disinfection of the operation area with 80% ethanol.

Induction of experimental autoimmune encephalitis

Mice were immunized subcutaneously with 250 µl emulsion containing 200 µg of purified recombinant MOG (N1-125) and complete Freund's adjuvant (Sigma-Aldrich, F5506) supplemented with 10 mg ml^{-1} *Mycobacterium tuberculosis* (H37RA, BD Difco, 231191). The mice received intraperitoneal (i.p.) injections with 200 ng pertussis toxin at day 0 and 2. After immunization, mice were weighed daily and neurological deficits were evaluated according to the following EAE score: 0, no clinical signs; 0.5, partial tail weakness; 1, tail paralysis; 1.5, gait instability or impaired righting ability; 2, hind limb paresis; 2.5, hind limb paresis with dragging of one foot; 3, total hind limb paralysis; 3.5, hind limb

paralysis and forelimb paresis; 4, hind limb and forelimb paralysis; and 5, death. The onset of disease was defined by the first day of neurological symptoms, the acute stage as 2–3 d following clinical onset and the chronic stage as 21/22 d following the onset of EAE.

Spinal cord laminectomy

Mice were imaged at the acute stage of EAE, 2 d after onset of disease (only animals with an EAE score ≥2.5 were included) and at onset plus 22 d for the chronic stage. The mice were anesthetized by i.p. injection of medetomidine (0.5 mg kg^{-1}), midazolam (5.0 mg kg^{-1}) and fentanyl (0.05 mg kg^{-1}) and tracheotomized and intubated to minimize breathing if needed. The dorsal spinal cord was surgically exposed as previously described[6]. In short, the skin was disinfected and incised along the spinal column. The lumbar-dorsal spinal cord was surgically exposed at the position of vertebrae L3 and L4 by performing a laminectomy and the surgical field was constantly superfused with pre-warmed artificial CSF (148.2 NaCl, 3.0 KCl, 1.4 $CaCl_2$, 0.8 $MgCl_2$, 0.8 Na_2HPO_4 and 0.2 NaH_2PO_4 in mM) to stay moisturized. The vertebral column was then position-fixed on a spinal clamping device (Narishige STS-a), allowing controlled movement in the *x*, *y* and *z* directions during the imaging session. A 3.5% agarose well was built up around the spinal opening and filled with artificial CSF. A standardized imaging protocol was used and at least three images were acquired in volume stacks penetrating up to 100 µm into the tissue from the spinal cord surface (meningeal level). Acute EAE was studied in animals that showed a clinical score ≥2.5 with confluent lesions present and image regions were defined based on the accumulation of infiltrated immune cells. During the imaging sessions, mice were kept under constant anesthesia and their breathing and reflexes were controlled every 30 min. Animals showing signs of traumatic damage after laminectomy were excluded from the analysis.

In vivo multi-photon and confocal imaging

Imaging of *Thy1*-PercevalHR mice. To measure the axonal ATP/ADP ratio, the genetically encoded ATP/ADP indicator PercevalHR was imaged using sequential two-photon excitation at 950 nm and 840 nm. Emission was collected simultaneously in the cyan and yellow channels using emission barrier filter pairs (bandwidth of 455–490 nm and 526–557 nm) on the Olympus MPE-resonant scanner system. Iodoacetic acid (IAA) (10 mM) or carbonyl cyanide *m*-chlorophenyl hydrazone (CCCP) (100 µM) at a final concentration was added to the imaging solution to obtain the baseline signal of the PercevalHR sensor. For imaging of the effects of Idh3a-tdTomato and Mdh2-tdTomato overexpression on the ATP/ADP ratio, we used the same settings as described above. In addition, tdTomato signals were recorded using a wavelength of 1,040 and collected in the red channel using a barrier filter of bandwidth 655–725 nm.

Imaging of AAV.PHPeB-hSyn:ATeam injected mice. To determine the axonal ATP level, the genetically encoded ATP sensor, ATeam, was imaged using a wavelength of 840 nm to excite mseCFP and cp173-mVenus fluorescent proteins. The emission signals were collected simultaneously in cyan and yellow channels using emission barrier filter pairs (bandwidth of 455–490 nm and 526–557 nm) on the Olympus MPE-resonant scanner system.

Imaging of *Thy1*-mitoTwitch2b × *Thy1*-OFP mice. To measure mitochondrial calcium levels in axons, the genetically encoded calcium indicator Twitch2b was excited using a wavelength of 840 nm to excite mCerulean3 and cpVenusCD fluorescent proteins simultaneously[22]. The signals were collected in the cyan and yellow channels. To reveal axonal morphology, the orange fluorescent signal was excited with a wavelength of 750 nm. The customized emission barrier filter pairs with bandwidths of 457-487 nm, 500–540 nm (GaAsP detectors) and 560–600 nm (RXD2 detector) were used on the Olympus MPE-FV1200 system. Images (12 bit) were acquired with a ×25/1.05 dipping cone water-immersion objective, a pixel size of 0.26 mm per pixel or smaller, a dwell time of 2.0 µs per pixel and a laser power of 30 mW measured in the back focal plane. Volume stacks penetrating ~50 µm into the dorsal spinal cord from the surface were acquired with a Z spacing of 1 µm.

Imaging of *Thy1*-mitoGrx-roGFP × *Thy1*-OFP mice. To determine the mitochondrial redox state in spinal axons, the genetically encoded redox indicator Grx-roGFP was sequentially excited using one-photon excitation at 405 and 488 nm wavelengths as previously described[19]. The signals were collected with emission barrier filter pairs (bandwidth 492–592 nm) in separate channels using a 50/50 beam splitter on an Olympus FV1000 confocal system. Smaller stacks were acquired with a Z spacing of 1 µm at a frame rate of 0.1–0.2 Hz.

Image processing and analysis

Images were analyzed with the open-source image analysis software ImageJ (Fiji, http://fiji.sc/Fiji) and Photoshop (Adobe). EAE lesions were identified according to the accumulation of infiltrated immune cells. The morphology of individual axons was traced and assessed through multi-stacks. To determine PercevalHR, ATeam or SypHer3s signals in axons, background intensities (non-axonal areas) of both channels were measured and subtracted for every axon in every experiment to create a background mask and pixel-by-pixel ratios were calculated from the mean over three regions of the same axon and further normalized to the mean value of the control mice to eliminate batch differences. For representative images that do not illustrate intensity variations, maximum intensity projections of image stacks were γ-adjusted to enhance the visibility of intermediate gray values and processed with a 'Despeckle' filter to lower the detector noise using Photoshop software (Adobe). To measure the redox state of a single mitochondrion or clusters of mitochondria signals in *Thy1*-mitoGrx-roGFP × *Thy1*-OFP, the mean intensity values were measured in the 405 and 488 nm channels as previously described[19]. The values for the two channels were divided (405/488 nm) to obtain a ratio related to the redox state of the sensor. This ratio was normalized to the mean value of the control mice. Mitochondrial morphology was quantified as the mitochondrial shape factor calculated by dividing the length by the width of a single mitochondrion as previously described[6]. To measure the calcium levels of a single mitochondrion or clusters of mitochondria in *Thy1*-mitoTwitch2b × *Thy1*-OFP, the mean intensity values were measured in the cyan and yellow channels. The FRET signal (YFP channel) was corrected by subtracting the measured crosstalk fraction of the CFP signal and is indicated as cFRET. The mitochondrial calcium levels were then expressed as the background-corrected cFRET:CFP ratio normalized to the mean value of healthy mice as previously established for FRET-based calcium sensors[14].

Mitochondrial isolation

Mitochondrial samples for mass spectrometry were prepared from adult male mice described in Fecher at al[23]. In brief, AAV.hSyn:Cre-injected control and EAE Mito*Tag* mice that thus express the GFP-labeled mitochondrial outer membrane in neurons were anesthetized with isoflurane and transcardially perfused with 1× PBS/heparin. The lumbar spinal cord was dissected, weighed and homogenized with a Dounce glass homogenizer using three complete up and down cycles with an A-type pestle in isolation buffer on ice. The sample was then transferred to a cell-disruption vessel and processed with nitrogen cavitation at 800 p.s.i. and under stirring at 60 r.p.m. for 10 min. After pressure release, a protease inhibitor (cOmplete, EDTA-free Protease Inhibitor Cocktail, Sigma-Aldrich, 5056489001) was added to the resulting tissue fraction, and subcellular sediments were removed through two times centrifugation at 600*g* for 10 min. The resulting post-nuclear tissue fraction was filtered through a 30-µm cell strainer. For immunopurification, the post-nuclear tissue fraction was diluted to a maximal concentration of 2 mg tissue per ml in immunopurification

buffer (IPB) and 50 µl microbeads coated with mouse IgG_1 subtype antibody (Miltenyi Biotec, 130-091-125) against GFP was added to the sample and incubated for 1 h at 4 °C on the shaker. Magnetic-activated cell sorting was applied to separate the microbead-coated mitochondria. The LS columns (Miltenyi Biotec, 130-042-401) were placed in a magnetic QuadroMACS separator (Miltenyi Biotec, 130-090-976) followed by the equilibration step with 3 ml IPB. The samples were applied to the column in repeating 3-ml steps and washed three times with IPB. The columns were removed from the magnetic separator and the microbead-coated mitochondria were gently flushed out with the plunger. Mitochondria were pelleted by centrifugation at 12,000*g* for 3 min at 4 °C and washed twice with isolation buffer (without BSA and EDTA) and the pellets were immediately stored at −20 °C for further experiments. Subsequently, the protein amount was determined using a BCA assay (Pierce BCA Protein Assay kit; Thermo Fisher Scientific, 23227) according to the manufacturer's instructions. BSA was used as the standard and the sample buffer was used to correct the measurement alterations caused by detergent or BSA.

Sample preparation for mass spectrometry

Mitochondria were immunocaptured from the spinal cord according to the above-described protocol. Samples were lysed in a modified RIPA buffer (1% Triton X-100, 0.5% sodium deoxycholate, 0.1% SDS, 150 mM NaCl, 5 mM EDTA and 50 mM Tris-HCl, pH 8). Cell debris and undissolved material were removed by centrifugation at 16,000*g* for 10 min at 4 °C. Protein concentrations were assessed using a BCA assay. A protein amount of 20 µg was further diluted with distilled water at a 1:2 ratio and 50 mM $MgCl_2$ was added to a final concentration of 10 mM and DNA/RNA was digested using 12.5 U benzonase. Disulfide bonds were reduced by adding dithiothreitol to a final concentration of 10 mM and incubation for 30 min at 37 °C. Cysteine alkylation was performed by adding iodoacetamide to a final concentration of 40 mM and incubation for 30 min at 24 °C in the dark. The alkylation step was quenched by adding 4 µl 200 mM dithiothreitol.

Protein digestion was performed using the single-pot, solid-phase, sample preparation (SP3) protocol[55]. Briefly, 10 µl of a 4 µg $µl^{-1}$ bead slurry of Sera-Mag SpeedBeads A and B (GE Healthcare) were added to 20 µg of alkylated protein lysate. Protein binding to the magnetic beads was achieved by adding acetonitrile to a final volume of 70% (v/v) and mixing at 1,200 r.p.m. at 24 °C for 30 min in a Thermomixer (Eppendorf). Magnetic beads were retained in a DynaMag-2 magnetic rack (Thermo Fisher Scientific) and the supernatant was discarded. Detergents were removed using four washing steps with 200 µl 80% (v/v) ethanol. Proteins were digested with 0.25 µg LysC (Promega, V1671) at 37 °C for 3 h followed by a second digestion step with 0.25 µg trypsin (Promega, V5111) for 16 h at room temperature. Tubes were placed in a magnetic rack and peptides were transferred to 0.22-µm Costar Spin-X filter tubes (Corning) to remove the remaining magnetic beads. Samples were dried by vacuum centrifugation. Finally, peptides were dissolved in 20 µl 0.1% (v/v) formic acid. Furthermore, the peptide concentration was estimated using the Qubit protein assay (Thermo Fisher, Q33211).

Liquid chromatography–tandem mass spectrometry data acquisition

Samples were analyzed on an Easy nLC-1200 nano UHPLC (Thermo Fisher Scientific) coupled online via a Nanospray Flex electrospray ion source (Thermo Fisher Scientific) equipped with a column oven (Sonation) to a Q-Exactive HF mass spectrometer (Thermo Fisher Scientific). An amount of 1.3 µg of peptides was separated on self-packed C18 columns (300 mm × 75 µm, ReproSilPur 120 C18-AQ, 1.9 µm; Dr Maisch) using a binary gradient of water (A) and acetonitrile (B) supplemented with 0.1% formic acid (gradient: 0 min, 2.4% B; 2 min, 4.8% B; 92 min, 24% B; 112 min, 35.2% B; 121 min, 60% B). Full mass spectrometry spectra were acquired at a resolution of 120,000 (automatic gain control target, 3×10^6). The 15 most-intense peptide ions were chosen for fragmentation by higher-energy collisional dissociation (resolution, 15,000; isolation width, 1.6 m/z; automatic gain control target, 1×10^5; normalized collision energy, 26%). A dynamic exclusion of 120 s was applied for fragment ion spectra acquisition. For EAE samples, two technical replicates were measured per sample.

Liquid chromatography–tandem mass spectrometry data analysis

The LC–MS/MS raw data were analyzed with the software MaxQuant (v.1.6.3.3 or v.1.6.10.43)[56]. The data was searched against a one gene per protein canonical database of *Mus musculus* downloaded from UniProt (downloaded 14 March 2019, 22,294 entries). Carbamidomethylation of cysteines was defined as fixed modification, whereas oxidation of methionines and acetylation of protein *N* termini were set as variable modifications. Peptide mass recalibration using the first search option with 20 ppm mass tolerance was enabled. For the main search, peptide and peptide fragment mass tolerances were set to 7 and 20 ppm, respectively. Peptide spectrum match and protein false discovery rates were set to 1% and false discovery rates were controlled using a forward and reverse concatenated database search approach. The option match between runs was enabled with a matching time window of 1.5 s. Protein label-free quantification (LFQ) was performed based on at least two ratio counts of unique peptides per protein. For EAE, LFQ intensities of technical replicates were averaged. If a protein was detected in <50% of the samples within one experimental group (EAE or control), all values were imputed with values drawn from a standard distribution with a mean value which was 2 × s.d. below the mean LFQ value of the entire dataset and a 0.3-fold s.d. of the overall s.d. of the dataset (to control for zero inflation). The remaining missing values (of proteins detected in >50% of the samples within one experimental group) were imputed by multiple imputations by chained equations (MICE, R package 'mice'). LFQ values were log_2-transformed. For subsequent analysis, LFQ values were treated as interval scale values. To test the similarity of samples within the respective experimental group and to identify outliers, principal-component analysis was performed. Subsequently, outliers were removed from further analyses. The first two principal components with their explained variance of each sample were visualized. To test whether a protein was differentially expressed between the EAE and control group, we calculated a Student's *t*-test and a fold change of the LFQ values between the experimental groups. To control type I error inflation, *P* values were corrected according to Bonferroni.

MitoCarta 2.0 (ref. 57) was used to annotate mitochondrial proteins as well as their sub-mitochondrial location. Gene set enrichment analysis was performed with the Python package nezzworker (https://github.com/engelsdaniel/nezzworker) with REACTOME (v.7.4) as a reference gene set library. Proteins which are members of gene sets that showed the most extreme NESs were further analyzed. To test whether mitochondrial, non-mitochondrial proteins and proteins from different mitochondrial respiratory chain complexes were equally abundant in EAE and control samples, one-way ANOVA was calculated to test for statistically significant differences between the mean LFQ values. To assess transcriptional changes of motor neurons in EAE, we re-analyzed previously published data from Schattling et al.[27], using a custom RDre script with the DESeq2 library. To assess the correlation of protein lifetime and the alterations of neuronal mitochondrial proteome, we extracted the protein half-lives dataset from Fornasiero et al.[41]. All analysis was performed in R studio (v.4.2.2) or Python (v.3, https://github.com/engelsdaniel/mitoproteomics).

Histology and immunofluorescence staining

Immunofluorescence staining on mouse tissues was performed as described in Fecher et al.[23] unless noted otherwise. Animals were anesthetized with isoflurane and perfused transcardially with 5,000 U ml^{-1} heparin (Sigma-Aldrich, H3149) in PBS followed by 4% PFA (Morphisto,

11762.01000) in phosphate buffer or 4% formalin (Sigma-Aldrich, HT501128). Tissues were kept in 4% PFA or 4% formalin overnight at 4 °C and subsequently cut using a vibratome (Leica). The tissue sections were permeabilized with 0.3% Triton X-100 (Sigma-Aldrich, X-100) and blocked using 2% fish gelatin (Sigma-Aldrich, G7765), 2% FBS (Thermo Fisher Scientific, 10500064) and 2% BSA (Sigma, A7030) in PBS for 1 h. Antigen retrieval procedures were applied to unmask antigens and epitopes. For this purpose, sections were treated with either 10 mM citrate buffer, pH 6.0, 10 mM EDTA buffer, pH 8.0, or citrate-EDTA (10 mM citric acid, 2 mM EDTA and 0.05% Tween20), pH 6.2 for 10 min at room temperature followed by 30 min at 90 °C and 30 min at 4 °C. The sections were further rinsed with 0.05% Tween20 (Sigma-Aldrich, P9416) before the blocking procedure. Primary antibodies were incubated overnight at 4 °C at a dilution of 1:400 (Mdh2, Novus Biologicals, NBP1-32259; Idh3a, Novus Biologicals, NBP1-32396; Idh2, Thermo Scientific, 702713; NeuN, clone A60, Sigma, MAB377) or 1:1,000 (RFP, Novus Biologicals, NBP1-97371 and GFP, Abcam, ab13970). The sections were incubated with secondary antibodies at a dilution of 1:1,000 for 2 h and mounted using Vectashield mounting medium (Vector Laboratories, H-1000) on the following day.

Heat-induced antigen retrieval was performed on PFA-fixed tissue following deparaffination for human tissue sections. After 10% FCS/PBS unspecific binding blockade, sections were incubated with primary antibodies in Dako Diluent (Dako, 52022) overnight at 4 °C. After washing with Wash Buffer (Dako, 53006) and autofluorescence removal treatment (Merck, 2160), secondary antibodies and DAPI (Life, D3571) at a dilution of 1:200 were incubated at room temperature for 1 h and further mounted with Fluoromount Mounting Medium (Sigma, F4680). The use of human samples followed institutional ethical guidelines and was approved by the ethics committee of the University of Geneva. Written informed consent to use autopsy samples for research purposes was obtained for all samples, with the exceptions of autopsies that were performed more than 20 years ago. In all cases, no samples were used from patients who refused involvement in research projects. Patient information is provided in Extended Data Table 1. Data from the human cortex are representative of two experiments performed on seven different cases.

Confocal imaging and image processing

Sections stained by immunofluorescence labeling to quantify mitochondrial proteins in neuronal somata, were imaged with an upright Olympus FV1000 confocal system equipped with ×10/0.4 air, ×20/0.85 and ×60/1.42 oil immersion objectives or a Leica SP8 equipped with ×20/0.75 HC PL APO CS2 and ×40/1.30 oil immersion HC PL APO CS2 objectives. Images were obtained using standard filter sets and processed with Fiji. For representative figure panels, different channels of image series were pseudo-color-coded in Fiji or Adobe Photoshop; schematics were created using BioRender.com. Contrast and brightness were equally adjusted across the entire image. For the panels displayed in Fig. 4 for intensity comparison, immunofluorescence images of both control and EAE *Thy1*-mitoRFP tissues were acquired with the same settings and were adjusted with the same processing parameters. In panels that do not primarily illustrate quantitative differences, γ was adjusted nonlinearly to enhance the visibility of low-intensity objects. Figures were assembled in Adobe Illustrator.

Human tissue sections were scanned using a whole slide scanner (PANNORAMIC P250 II, 3DHistech). Regions of interest were manually selected using SlideViewer software (v.2.3, 3DHistech) and exported as individual images for further processing using a custom rule-based script in Definiens Developer XD (v.2.7, Definiens). In short, specific signals for each marker were detected based on their respective intensity and ratio to tissue background intensity. NF70 (neurofilament) was detected first and Idh3a detection was restricted to the inside of NF70-positive structures. The total area was quantified for each marker. Additionally, mean intensities were exported for each object individually. For quantification of TCA cycle enzymes in mouse axons, we followed the same approach both for reasons of consistency, but also because mitochondria in axons can be difficult to stain in non-paraffin-embedded tissue. For this, slides of *Thy1*-mitoRFP mice stained with NF70 together with the mitochondrial markers Mhd2, Idh2 or Idh3a were imaged on Leica SP8 with ×40/1.30 oil immersion using standard filter sets and processed with Fiji. Notably, RFP fluorescence is abolished in this protocol, so independent masking of mitochondria based on a mitochondrial transgene or staging of FAD were not possible in this dataset. Image analysis was further performed in Visiopharm (v.2021.09). In summary, NF70-positive structures were detected and taken as the reference regions. Mitochondrial marker-positive puncta were then detected by a 120% intensity cutoff and a minimum size 4 pixel cutoff and quantified strictly within NF70-positive structures. The total area was quantified for NF-positive structures and marker-positive puncta, with the ratio representing 'occupancy'. Within the thus defined mitochondrial voxel, the mean intensity value for each individual object was quantified and the integrated density represents the sum of the values of the pixels in the image or selection, equivalent to the product of occupancy and mean intensities. Data were processed using R (v.4.2.2, R-project.org).

Sequential cytochrome c oxidase histochemistry and immunofluorescence histochemistry

To assess COX activity in single axons, COX histochemistry was combined with immunofluorescence histochemistry with a primary antibody against OFP followed by a directly conjugated secondary antibody. This sequential technique was performed in the same tissue section and has already been described and validated in previous studies[5,24,58]. The COX medium consisted of 100 µM cytochrome c, 4 mM diaminobenzidine tetrahydrochloride and 20 µg ml^{-1} catalase in 0.1 M phosphate buffer at pH 7.0. Cryosections were incubated at 37 °C for 30 min and washed in PBS. The cryosections were processed through the immunofluorescent histochemistry steps as mentioned above. The sequentially stained sections were mounted in glycerol with Hoechst nuclear stain and stored at −20 °C until required for imaging by the Zeiss Imager Z1 Apotome 2 microscope.

To assess COX activity in axons, a mask of the individual axon identified by the fluorescent labeling of OFP was generated in ImageJ and superimposed onto the brightfield image of COX histochemistry. The total area occupied by COX active elements within a single axon was determined as a percentage of the axonal area. Twenty axons (at least 25 µm in length) per region were randomly selected from each animal for quantitation. Assessors were blinded by coding the axons in ascending numerical order.

Metabolic modeling

Metabolic modeling was performed using the QSM data analysis platform provided by Doppelganger Biosystem, using the mass spectrometry analysis described above for *MitoTag*-derived neuronal mitochondria from acute (2–3 d following clinical onset) EAE versus controls (n = 6 and 5 mice, respectively). A detailed description of the approach used can be found in Berndt et al.[46]. In brief, the QSM kinetic model includes the major cellular metabolic pathways of mitochondrial energy metabolism and glycolysis, as well as key electrophysiological processes at the inner mitochondrial membrane (membrane transport of various ions, mitochondrial membrane potential, generation and utilization of the proton motive force). First-order differential equations govern the time-dependent variations of model variables (concentration of metabolites and ions), with time-variations of small ions modeled by kinetic equations of the Goldman–Hodgkin–Katz type. The model uses numerical values for kinetic parameters of the enzymatic rate laws from reported kinetic studies of the isolated enzyme, whereas maximal enzyme activities (v_{max} values) are estimated based on functional characteristics and metabolite

concentrations of a health neuronal tissue[46]. To establish individual metabolic models, the approach uses the protein intensity profiles of quantitative shotgun proteomics of *MitoTag*-derived neuronal mitochondria. The maximal activities of enzymes and transporters are scaled, exploiting the fact that the maximal activity of an enzyme is proportional to the abundance of the enzyme protein via υ_{max}(EAE) = υ_{max}(normal) × (E(EAE) / E(mean control)). υ_{max}(normal) denotes the maximal activity for a given enzyme as used by Berndt et al.[46], E(EAE) denotes the protein abundance measured of enzyme E in a given EAE sample and E(mean control) represents the mean protein abundance of an enzyme E averaged across the control sample measurements. Applying the model involves tailored quality control (QC), which evaluates both the number of proteins of interest found (QC score) and the number of metabolic processes associated with the enzymes found (QSM score), which indicated good suitability for applying the QSM kinetic model (QC > 90%; QSM > 100%, with 75% being the standard cutoff). To evaluate energetic capacities, the model calculates the changes of metabolic state due to increasing the rate of ATP consumption above the resting value, with the ATP consumption rate being modeled by a generic hyperbolic rate law of the form $\upsilon_{ATP} = k_{load} \times (ATP / ATP + K_m)$. To model increased 'metabolic load', the parameter k_{load} was increased in steps until convergence of the ATP production rate to its maximal value.

Statistics and reproducibility

All experiments in this study include at least three biological replicates, except in Extended Data Fig. 2e. The number of biological replicates (n) is mentioned for each experiment in the figure legend. No statistical methods were used to predetermine sample size, but our sample sizes are similar to those reported in previous publications[6,14,17,23]. Data collection and analysis were performed blind to the conditions of the experiment, unless this was not possible due to an obvious disease or labeling phenotype. Statistical analysis was performed using Microsoft Excel software and GraphPad Prism (GraphPad Software, v.7.0). Sample sizes were chosen according to previous in vivo imaging studies of spinal axons[6,14]. Normality of distribution was assessed with the Shapiro–Wilk test. When normal distribution was confirmed, a two-tailed Student's *t*-test was applied for two groups comparison and one-way ANOVA followed by Bonferroni's or Turkey's post hoc comparison was used for more than two groups. The Kruskal–Wallis test followed by Dunn's multiple comparisons test or Mann–Whitney *U*-test was used where normal distribution could not be confirmed. Obtained *P* values were stated as significance levels in the figure legends (****$P < 0.001$, ***$P < 0.005$; **$P < 0.01$; *$P < 0.05$; NS, not significant). Data are expressed as the mean and the error bars indicate s.e.m. unless specified otherwise in the legends.

Reporting summary

Further information on research design is available in the Nature Portfolio Reporting Summary linked to this article.

Data availability

All data are available in the manuscript or the supplementary materials. Raw data are available upon reasonable request to the corresponding authors. The transgenic mouse lines (*Thy1*-mitoTwitch2b and *Thy1*-PercevalHR) and the plasmids (pAAV.hSyn:Idh3a.P2A.tdTomato, pAAV.hSyn:mMdh2.P2A.tdTomato, pAAV.hSyn:Ateam1.03 and pAAV.hSyn:SypHer3s) are available on request. All proteomic datasets generated within this study are deposited online to the ProteomeXchange Consortium via the PRIDE partner repository with the dataset identifier PXD032363 and at the GitHub repository (https://github.com/engelsdaniel/mitoproteomics). The codes used to reanalyze the single-cell data (Fig. 3f) from Schattling et al. are publicly available on the GitHub repository (https://github.com/engelsdaniel/mitoproteomics). Source data are provided with this paper.

References

1. Friese, M. A., Schattling, B. & Fugger, L. Mechanisms of neurodegeneration and axonal dysfunction in multiple sclerosis. *Nat. Rev. Neurol.* **10**, 225–238 (2014).
2. Mahad, D. H., Trapp, B. D. & Lassmann, H. Pathological mechanisms in progressive multiple sclerosis. *Lancet Neurol.* **14**, 183–193 (2015).
3. Absinta, M., Lassmann, H. & Trapp, B. D. Mechanisms underlying progression in multiple sclerosis. *Curr. Opin. Neurol.* **33**, 277–285 (2020).
4. Misgeld, T. & Schwarz, T. L. Mitostasis in neurons: maintaining mitochondria in an extended cellular architecture. *Neuron* **96**, 651–666 (2017).
5. Mahad, D. J. et al. Mitochondrial changes within axons in multiple sclerosis. *Brain* **132**, 1161–1174 (2009).
6. Nikic, I. et al. A reversible form of axon damage in experimental autoimmune encephalomyelitis and multiple sclerosis. *Nat. Med.* **17**, 495–499 (2011).
7. Sadeghian, M. et al. Mitochondrial dysfunction is an important cause of neurological deficits in an inflammatory model of multiple sclerosis. *Sci. Rep.* **6**, 33249 (2016).
8. Campbell, G. R. et al. Mitochondrial DNA deletions and neurodegeneration in multiple sclerosis. *Ann. Neurol.* **69**, 481–492 (2011).
9. Witte, M. E., Mahad, D. J., Lassmann, H. & van Horssen, J. Mitochondrial dysfunction contributes to neurodegeneration in multiple sclerosis. *Trends Mol. Med.* **20**, 179–187 (2014).
10. Cree, B. A. C. et al. Safety and efficacy of MD1003 (high-dose biotin) in patients with progressive multiple sclerosis (SPI2): a randomised, double-blind, placebo-controlled, phase 3 trial. *Lancet Neurol.* **19**, 988–997 (2020).
11. Rosenkranz, S. C. et al. Enhancing mitochondrial activity in neurons protects against neurodegeneration in a mouse model of multiple sclerosis. *eLife* **10**, e61798 (2021).
12. Pathak, D., Berthet, A. & Nakamura, K. Energy failure: does it contribute to neurodegeneration. *Ann. Neurol.* **74**, 506–516 (2013).
13. Tantama, M., Martinez-Francois, J. R., Mongeon, R. & Yellen, G. Imaging energy status in live cells with a fluorescent biosensor of the intracellular ATP-to-ADP ratio. *Nat. Commun.* **4**, 2550 (2013).
14. Witte, M. E. et al. Calcium Influx through plasma-membrane nanoruptures drives axon degeneration in a model of multiple sclerosis. *Neuron* **101**, 615–624 (2019).
15. Imamura, H. et al. Visualization of ATP levels inside single living cells with fluorescence resonance energy transfer-based genetically encoded indicators. *Proc. Natl Acad. Sci. USA* **106**, 15651–15656 (2009).
16. Ermakova, Y. G. et al. SypHer3s: a genetically encoded fluorescent ratiometric probe with enhanced brightness and an improved dynamic range. *Chem. Commun.* **54**, 2898–2901 (2018).
17. Sorbara, C. D. et al. Pervasive axonal transport deficits in multiple sclerosis models. *Neuron* **84**, 1183–1190 (2014).
18. Kawachi, I. & Lassmann, H. Neurodegeneration in multiple sclerosis and neuromyelitis optica. *J. Neurol. Neurosurg. Psychiatry* **88**, 137–145 (2017).
19. Breckwoldt, M. O. et al. Multiparametric optical analysis of mitochondrial redox signals during neuronal physiology and pathology in vivo. *Nat. Med.* **20**, 555–560 (2014).
20. Brill, M. S., Lichtman, J. W., Thompson, W., Zuo, Y. & Misgeld, T. Spatial constraints dictate glial territories at murine neuromuscular junctions. *J. Cell Biol.* **195**, 293–305 (2011).
21. Giorgi, C., Marchi, S. & Pinton, P. The machineries, regulation and cellular functions of mitochondrial calcium. *Nat. Rev. Mol. Cell Biol.* **19**, 713–730 (2018).

22. Thestrup, T. et al. Optimized ratiometric calcium sensors for functional in vivo imaging of neurons and T lymphocytes. *Nat. Methods* **11**, 175–182 (2014).
23. Fecher, C. et al. Cell-type-specific profiling of brain mitochondria reveals functional and molecular diversity. *Nat. Neurosci.* **22**, 1731–1742 (2019).
24. Zambonin, J. et al. Identification and investigation of mitochondria lacking cytochrome c oxidase activity in axons. *J. Neurosci. Methods* **192**, 115–120 (2010).
25. Martinez-Reyes, I. & Chandel, N. S. Mitochondrial TCA cycle metabolites control physiology and disease. *Nat. Commun.* **11**, 102 (2020).
26. Owen, O. E., Kalhan, S. C. & Hanson, R. W. The key role of anaplerosis and cataplerosis for citric acid cycle function. *J. Biol. Chem.* **277**, 30409–30412 (2002).
27. Schattling, B. et al. Bassoon proteinopathy drives neurodegeneration in multiple sclerosis. *Nat. Neurosci.* **22**, 887–896 (2019).
28. Soundar, S., Park, J. H., Huh, T. L. & Colman, R. F. Evaluation by mutagenesis of the importance of 3 arginines in α, β, and γ subunits of human NAD-dependent isocitrate dehydrogenase. *J. Biol. Chem.* **278**, 52146–52153 (2003).
29. Gabriel, J. L., Zervos, P. R. & Plaut, G. W. Activity of purified NAD-specific isocitrate dehydrogenase at modulator and substrate concentrations approximating conditions in mitochondria. *Metabolism* **35**, 661–667 (1986).
30. Al-Khallaf, H. Isocitrate dehydrogenases in physiology and cancer: biochemical and molecular insight. *Cell Biosci.* **7**, 37 (2017).
31. Anderson, N. M., Mucka, P., Kern, J. G. & Feng, H. The emerging role and targetability of the TCA cycle in cancer metabolism. *Protein Cell* **9**, 216–237 (2018).
32. Golub, D. et al. Mutant isocitrate dehydrogenase inhibitors as targeted cancer therapeutics. *Front. Oncol.* **9**, 417 (2019).
33. Hvinden, I. C., Cadoux-Hudson, T., Schofield, C. J. & McCullagh, J. S. O. Metabolic adaptations in cancers expressing isocitrate dehydrogenase mutations. *Cell Rep. Med.* **2**, 100469 (2021).
34. Liu, S., Cadoux-Hudson, T. & Schofield, C. J. Isocitrate dehydrogenase variants in cancer: cellular consequences and therapeutic opportunities. *Curr. Opin. Chem. Biol.* **57**, 122–134 (2020).
35. Molenaar, R. J., Maciejewski, J. P., Wilmink, J. W. & van Noorden, C. J. F. Wild-type and mutated IDH1/2 enzymes and therapy responses. *Oncogene* **37**, 1949–1960 (2018).
36. Chan, K. Y. et al. Engineered AAVs for efficient noninvasive gene delivery to the central and peripheral nervous systems. *Nat. Neurosci.* **20**, 1172–1179 (2017).
37. Trapp, B. D. & Stys, P. K. Virtual hypoxia and chronic necrosis of demyelinated axons in multiple sclerosis. *Lancet Neurol.* **8**, 280–291 (2009).
38. Nijland, P. G. et al. Differential expression of glucose-metabolizing enzymes in multiple sclerosis lesions. *Acta Neuropathol. Commun.* **3**, 79 (2015).
39. Vasan, K., Werner, M. & Chandel, N. S. Mitochondrial metabolism as a target for cancer therapy. *Cell Metab.* **32**, 341–352 (2020).
40. Motori, E. et al. Neuronal metabolic rewiring promotes resilience to neurodegeneration caused by mitochondrial dysfunction. *Sci. Adv.* **6**, eaba8271 (2020).
41. Fornasiero, E. F. et al. Precisely measured protein lifetimes in the mouse brain reveal differences across tissues and subcellular fractions. *Nat. Commun.* **9**, 4230 (2018).
42. Bomba-Warczak, E., Edassery, S. L., Hark, T. J. & Savas, J. N. Long-lived mitochondrial cristae proteins in mouse heart and brain. *J. Cell Biol.* **220**, e202005193 (2021).
43. Trapp, B. D. & Nave, K. A. Multiple sclerosis: an immune or neurodegenerative disorder. *Annu. Rev. Neurosci.* **31**, 247–269 (2008).
44. Sheng, Z. H. The interplay of axonal energy homeostasis and mitochondrial trafficking and anchoring. *Trends Cell Biol.* **27**, 403–416 (2017).
45. Trevisiol, A. et al. Monitoring ATP dynamics in electrically active white matter tracts. *eLife* **6**, e24241 (2017).
46. Berndt, N., Kann, O. & Holzhutter, H. G. Physiology-based kinetic modeling of neuronal energy metabolism unravels the molecular basis of NAD(P)H fluorescence transients. *J. Cereb. Blood Flow. Metab.* **35**, 1494–1506 (2015).
47. Cunnane, S. C. et al. Brain energy rescue: an emerging therapeutic concept for neurodegenerative disorders of ageing. *Nat. Rev. Drug Discov.* **19**, 609–633 (2020).
48. Motte, J. & Gold, R. High-dose biotin in multiple sclerosis: the end of the road. *Lancet Neurol.* **19**, 965–966 (2020).
49. Sun, P., Bai, T., Ma, T. & Ding, J. Molecular mechanism of the dual regulatory roles of ATP on the αγ heterodimer of human NAD-dependent isocitrate dehydrogenase. *Sci. Rep.* **10**, 6225 (2020).
50. Denton, R. M. Regulation of mitochondrial dehydrogenases by calcium ions. *Biochim. Biophys. Acta* **1787**, 1309–1316 (2009).
51. Upadhyay, V. A., Brunner, A. M. & Fathi, A. T. Isocitrate dehydrogenase (IDH) inhibition as treatment of myeloid malignancies: Progress and future directions. *Pharmacol. Ther.* **177**, 123–128 (2017).
52. Licht-Mayer, S. et al. Enhanced axonal response of mitochondria to demyelination offers neuroprotection: implications for multiple sclerosis. *Acta Neuropathol.* **140**, 143–167 (2020).
53. May, J. L. et al. IDH3α regulates one-carbon metabolism in glioblastoma. *Sci. Adv.* **5**, eaat0456 (2019).
54. Wang, M., Misgeld, T. & Brill, M. S. Neural labeling and manipulation by neonatal intraventricular viral injection in mice. *STAR Protoc.* **3**, 101081 (2022).
55. Hughes, C. S. et al. Single-pot, solid-phase-enhanced sample preparation for proteomics experiments. *Nat. Protoc.* **14**, 68–85 (2019).
56. Cox, J. et al. Accurate proteome-wide label-free quantification by delayed normalization and maximal peptide ratio extraction, termed MaxLFQ. *Mol. Cell Proteom.* **13**, 2513–2526 (2014).
57. Calvo, S. E., Clauser, K. R. & Mootha, V. K. MitoCarta2.0: an updated inventory of mammalian mitochondrial proteins. *Nucleic Acids Res.* **44**, D1251–D1257 (2016).
58. Mahad, D. J. et al. Detection of cytochrome c oxidase activity and mitochondrial proteins in single cells. *J. Neurosci. Methods* **184**, 310–319 (2009).
59. Jassal, B. et al. The reactome pathway knowledgebase. *Nucleic Acids Res.* **48**, D498–D503 (2020).
60. Gillespie, M. et al. The reactome pathway knowledgebase 2022. *Nucleic Acids Res.* **50**, D687–D692 (2022).

Acknowledgements

We thank A. Schmalz, J. Schmitt, K. Plesniar, B. Fiedler, Y. Hufnagel and A. Berghofer for excellent technical assistance and D. Matzek, B. Stahr, M. Korica, N. and M. Budak for animal husbandry. We also acknowledge A. Marti Pastor and Y. Hufnagel for help with *MitoTag* isolations, K. Dyar (Helmholtz Center Munich) for advice on metabolomics, O. Griesbeck (Max Planck Institute of Neurobiology) for constructs, J. Lichtman (Harvard University) for *Thy1*-OFP mice and C. de la Rosa (BMC/LMU) for support on PHP.eB virus establishment.

This project was supported by the Deutsche Forschungsgemeinschaft (DFG) via TRR 274/1 (projects B03, C02, C05, Z01, Z02, ID 408885537). Work in M. Kerschensteiner's laboratory is further financed through grants from the DFG (TRR128, project B10 and B13;

TRR152, project P27, ID 239283807), the European Research Council (ERC) under the European Union's Seventh Framework Program (FP/2007-2013; ERC grant agreement no. 310932), the German Federal Ministry of Research and Education (Competence Network Multiple Sclerosis) and the 'Verein Therapieforschung für MS-Kranke e.V.'. Work in the laboratory of T.M. is supported by the DFG (CRC870 A11-ID 118803580, Mi 694/8-1, Mi 694/9-1 A03-ID 428663564, FOR Immunostroke) and the ERC under the European Union's Seventh Framework Program (FP/2007-2013; ERC grant agreement no. 616791). T.M. also acknowledges a Pioneer Grant from Doppelganger Biosystem GmbH for metabolic modeling. T.M. and S.F.L. are members of and supported by the German Center for Neurodegenerative Diseases. High-resolution microscopy was supported via a DFG instrumentation grant (INST95/1755-1 FUGG, ID 518284373). M. Kerschensteiner and T.M. were further supported by the DFG through a common grant (Ke 774/5-1/Mi 694/7-1) and, together with S.F.L., F.P. and F.M.B., receive support from the Munich Center for Systems Neurology (SyNergy EXC 2145; project ID 390857198). D. Merkler is supported by the Swiss National Science Foundation (310030B_201271 & 310030_185321) and the ERC (865026). M.O.B. was recipient of a doctoral fellowship from the Gertrud Reemtsma Foundation and supported by the Emmy Noether Program of the DFG (BR 6153/1-1). G.L. and L.T. were supported by EMBO Fellowships, G.L. further received a Swiss National Science Foundation fellowship. Y.-H.T. received support via the TUM Graduate School via the PhD Program 'Medical Life Sciences and Technology'. I.E. and C.F. were supported via the Munich School of Systemic Neurosciences (GSC 82, ID 24184143).

Author contributions

M. Kerschensteiner and T.M. conceived and designed the experiments. Y.-H.T. performed in vivo imaging and disease modeling experiments, with contributions from G.L. for mitochondrial calcium and redox imaging. C.F., G.L, D.T., Y.-H.T., R.N. and M.O.B. established and characterized mouse lines for in vivo imaging, L.T., C.F. and Y.-H.T. established, supported and performed the MitoTag analysis, for which S.A.M. and S.F.L. conducted the proteomic analysis. D.E. performed the bioinformatics analysis with input from S.A.M. and S.F.L. M. Kreutzfeldt, I.W. and D. Merkler conducted histological analysis of MS. Y.-H.T., I.E. and S.-N.G. performed mouse histology and S.L.-M. and D. Mahad contributed the COX IV assay in EAE. A.K. and Y.-H.T. designed and cloned AAV vectors. A.A. and F.M.B. supported the generation of the PHP.eB viruses. N.P.dM. and F.P. supported bioenergics analyses. Y.-H.T. coordinated and contributed data analysis across all experimental approaches and designed the final data representation with input from M. Kerschensteiner and T.M. Y.-H.T., M. Kerschensteiner and T.M. wrote the paper with input from all authors.

Competing interests

The authors declare no competing interests.

Additional information

Extended data is available for this paper at https://doi.org/10.1038/s42255-023-00838-3.

Supplementary information The online version contains supplementary material available at https://doi.org/10.1038/s42255-023-00838-3.

Correspondence and requests for materials should be addressed to Martin Kerschensteiner or Thomas Misgeld.

Peer review information *Nature Metabolism* thanks Zu-Hang Sheng, Peter Calabresi and the other, anonymous, reviewers for their contribution to the peer review of this work. Primary handling editor: Alfredo Giménez-Cassina, in collaboration with the *Nature Metabolism* team.

Reprints and permissions information is available at www.nature.com/reprints.

Publisher's note Springer Nature remains neutral with regard to jurisdictional claims in published maps and institutional affiliations.

[1]Institute of Clinical Neuroimmunology, University Hospital, Ludwig-Maximilians Universität (LMU) München, Munich, Germany. [2]Biomedical Center (BMC), Faculty of Medicine, Ludwig-Maximilians Universität München, Martinsried, Germany. [3]Institute of Neuronal Cell Biology, Technical University of Munich, Munich, Germany. [4]German Center for Neurodegenerative Diseases (DZNE), Munich, Germany. [5]Neuroproteomics, School of Medicine, Klinikum rechts der Isar, Technical University of Munich, Munich, Germany. [6]Centre for Clinical Brain Sciences, University of Edinburgh, Edinburgh, UK. [7]Department of Pathology and Immunology, Division of Clinical Pathology, University & University Hospitals of Geneva, Geneva, Switzerland. [8]Institute for Diabetes and Obesity, Helmholtz Zentrum München, Munich, Germany. [9]Transgenic Core Facility, Max Planck Institute of Molecular Cell Biology and Genetics, Dresden, Germany. [10]Munich Cluster for Systems Neurology (SyNergy), Munich, Germany. [11]Present address: Novartis Institutes for BioMedical Research (NIBR), Basel, Switzerland. [12]Present address: Department of Cell Biology and Physiology, Washington University in St Louis, St. Louis, MO, USA. [13]Present address: Department of Neuroradiology, University Hospital Heidelberg, Heidelberg, Germany. [14]These authors jointly supervised this work: Martin Kerschensteiner, Thomas Misgeld. ✉e-mail: martin.kerschensteiner@med.uni-muenchen.de; thomas.misgeld@tum.de

https://doi.org/10.1038/s42255-023-00838-3

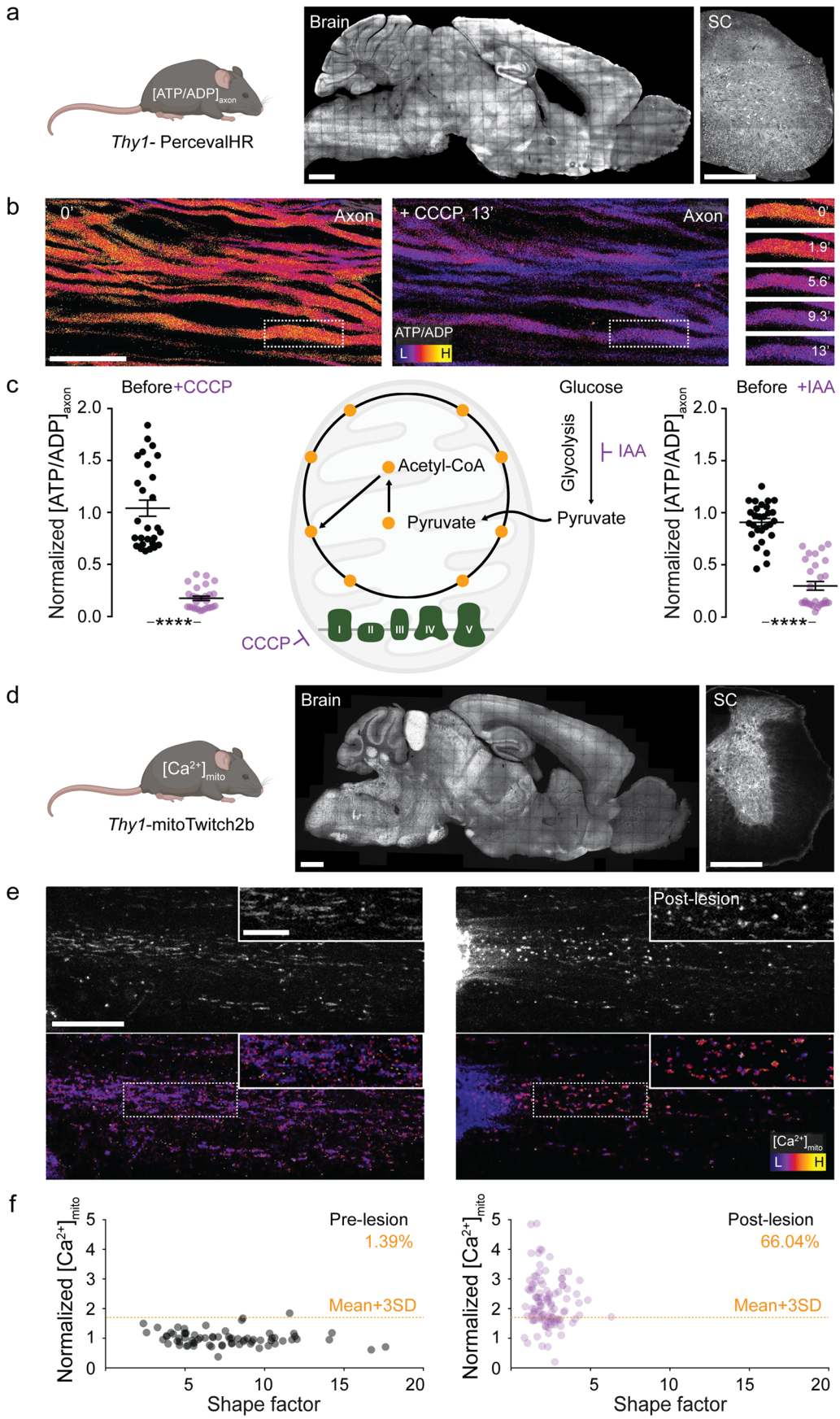

Extended Data Fig. 1 | See next page for caption.

https://doi.org/10.1038/s42255-023-00838-3

Extended Data Fig. 1 | Transgenic mouse lines to measure neuronal ATP/ADP ratio and mitochondrial calcium. (a) CNS expression pattern of *Thy1*-PercevalHR mice. Confocal images of sagittal brain (left) and transverse spinal cord (SC) section (right; grayscale LUT; λ_{ex} 488 nm). (b) Maximum intensity projections of *in vivo* multi-photon image stacks of axons in a *Thy1*-PercevalHR mouse spinal cord before (left) and after (middle) CCCP application. Individual frames in boxed area spanning 0 to 13 minutes after CCCP application (right). Ratiometric $[ATP/ADP]_{axon}$ LUT (λ_{ex} ratio 950 nm/840 nm). (c) $[ATP/ADP]_{axon}$ of single axons before and after CCCP (100 µM, 15 min; left) and IAA (10 mM, 15 min; right) application, which interfere with oxidative phosphorylation and glycolysis, respectively. Values are normalized to mean of control. Mean ± s.e.m.; n = 27 axons from three mice with CCCP and 28 axons from three mice with IAA, compared by Mann-Whitney test, $p = 10^{-15}$ and 7.1×10^{-13}, respectively. Scale bars: 1000 µm in a, left; 500 µm in a, right; 25 µm in b. ****, $p < 0.001$. (d) CNS expression pattern of *Thy1*-mitoTwitch2b mice. Confocal images of sagittal brain (left) and transverse SC section (right; YFP channel using grayscale LUT). (e) Maximum intensity projections of *in vivo* multi-photon image stacks of axonal mitochondria in a *Thy1*-mitoTwitch2b mouse spinal cord before (left) and after (right) laser lesion. Top: YFP channel using grayscale LUT; Bottom: Ratiometric $[Ca^{2+}]_{mito}$ LUT (YFP/CFP emission ratio). Insets: Details from respective panels. (f) $[Ca^{2+}]_{mito}$ of axonal mitochondria before and after laser lesion (n > 150 mitochondria from 8 axons, three mice). Percentages indicate the fraction of axons with $[Ca^{2+}]_{mito}$ > mean + 3 SD of values pre-lesion (orange line). Scale bars: 1000 µm in d, left; 500 µm in d, right; 20 µm in e; 10 µm in inset. See source data for individual data points and further statistical parameters. Illustration created with BioRender.

https://doi.org/10.1038/s42255-023-00838-3

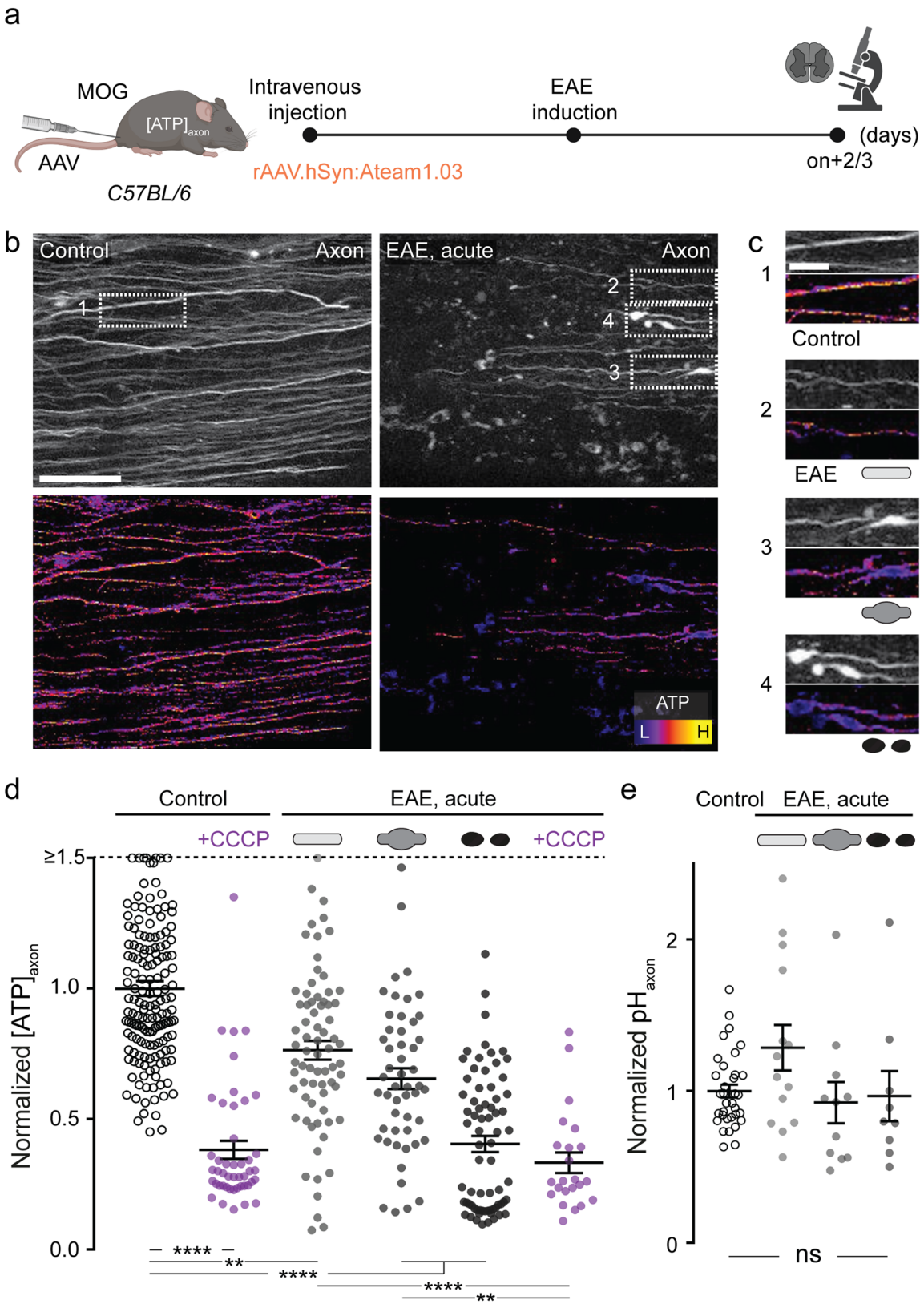

Extended Data Fig. 2 | See next page for caption.

https://doi.org/10.1038/s42255-023-00838-3

Extended Data Fig. 2 | Early axonal ATP deficits measured using ATeam in EAE. (**a**) Experimental design for axonal ATP level measurement in experimental autoimmune encephalomyelitis (EAE). (**b**) Maximum intensity projections of *in vivo* multi-photon image stacks of spinal cord axons of control (left) and acute EAE (right) in AAV.PHPeB.hSyn:ATeam injected C57BL/6 mice. Top: Grayscale look-up table (LUT; λ_{ex} 840 nm). Bottom: Ratiometric $[ATP]_{axon}$ LUT (YFP/CFP emission ratio). (**c**) Details from b. Top to bottom: $[ATP]_{axon}$ images of control axon in healthy spinal cord and normal-appearing, swollen, and fragmented axons in acute EAE. (**d**) $[ATP]_{axon}$ of single axons in healthy and EAE mice normalized to mean of controls. Mean ± s.e.m.; n = 157 axons from three control and 195 axons from four EAE mice compared by Kruskal-Wallis and Dunn's multiple comparison test; values above 1.5 lined up on the "≥1.5" dashed line, $p < 0.001$, control versus control + CCCP; $p = 0.001$, 5.4×10^{-7}, < 0.001, control versus stage 0, 1 and 2, respectively; $p = 6.1 \times 10^{-6}$, 0.0057, > 0.9999, EAE + CCCP versus stage 0, 1 and 2, respectively. (**e**) $[pH]_{axon}$ of single axons measured by using SypHer3s sensor in control and acute EAE mice normalized to mean of controls. Mean ± s.e.m.; n = 34 axons from two control and 34 axons from two EAE mice, compared Kruskal-Wallis and Dunn's multiple comparison test, $p > 0.9999$, control versus stage 0, 1 and 2, respectively. Scale bars: 25 µm in b; 10 µm in c. **, $p < 0.01$; ****, $p < 0.001$. See source data for individual data points and further statistical parameters. Illustration created with BioRender.

https://doi.org/10.1038/s42255-023-00838-3

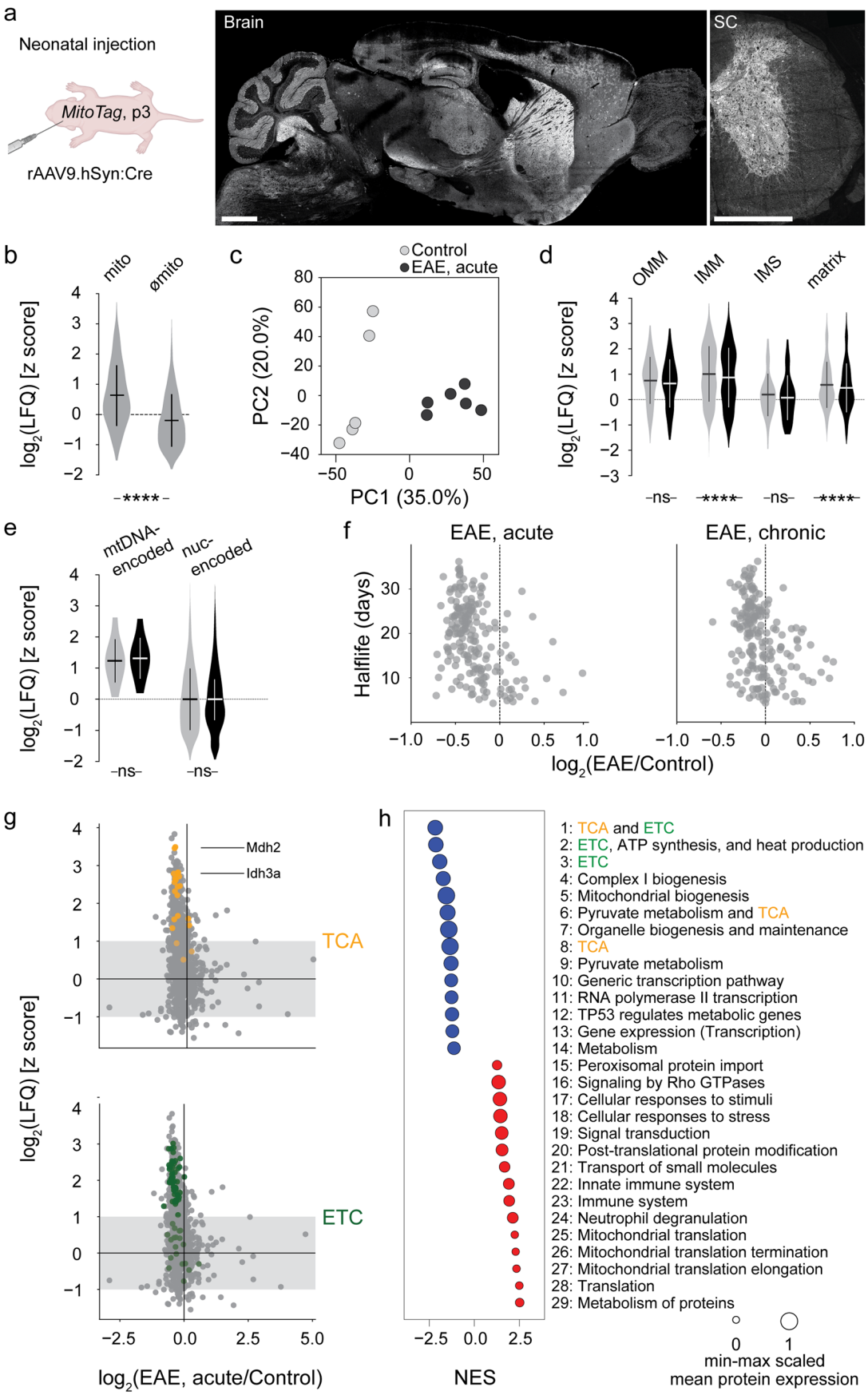

Extended Data Fig. 3 | See next page for caption.

https://doi.org/10.1038/s42255-023-00838-3

Extended Data Fig. 3 | Proteomics analysis of neuronal mitochondria in EAE. (**a**) CNS expression pattern of *MitoTag* mouse injected with rAAV. hSyn:Cre. Confocal images of the sagittal brain (left) and transverse spinal cord (SC) section (right; grayscale LUT; λ_{ex} 488 nm). (**b**) Relative expression level (z-score for label-free quantification intensity, LFQ) of proteins quantified by mass spectrometry in *MitoTag* isolations that are annotated as mitochondrial proteins in MitoCarta 2.0[57] (mito) or not (ϕmito), $p = 6.14 \times 10^{-105}$ (**c**) Principal component analysis of MitoTag proteomics control and acute EAE samples. (**d**) Expression level (log_2 of LFQ) of proteins annotated in MitoCarta 2.0[57] to reside in different mitochondrial subcompartments in control (gray) and acute EAE (black), including outer membrane (OMM, p = 0.075), inner membrane (IMM, p = 0.0013), intermembrane space (IMS, p = 0.26) and matrix (p = 0.00012) relative to all MitoCarta proteins. (**e**) Same as d, but for nuclear- vs. mitochondrial DNA-encoded proteins, p = 0.59 and 0.98, respectively. (**f**) Fold change (log_2 of LFQ ratio of EAE over Control) versus protein half-life (as measured in Fornasiero et al[41]). (**g**) Location of the TCA cycle (top, orange) and electron transport chain (ETC; bottom, green) proteins on the correlation plot of protein abundance (z score of label-free quantification values, LFQ) vs. fold change (log_2 of LFQ ratio acute EAE over control). The vertical lines indicate the mean ± 1 SD, compared using a two-tailed, unpaired Student's t-test. Biological replicates: n ≥ 3. (**h**) Annotations of the most regulated pathways (Reactome[59,60], version 7.4) in *MitoTag* proteomes of neuronal mitochondria in acute EAE. Scale bars: 1000 µm in a, left; 500 µm in a, right. ****, p < 0.001. See source data for individual data points and further statistical parameters. See source data for individual data points and further statistical parameters. Illustration created with BioRender.

https://doi.org/10.1038/s42255-023-00838-3

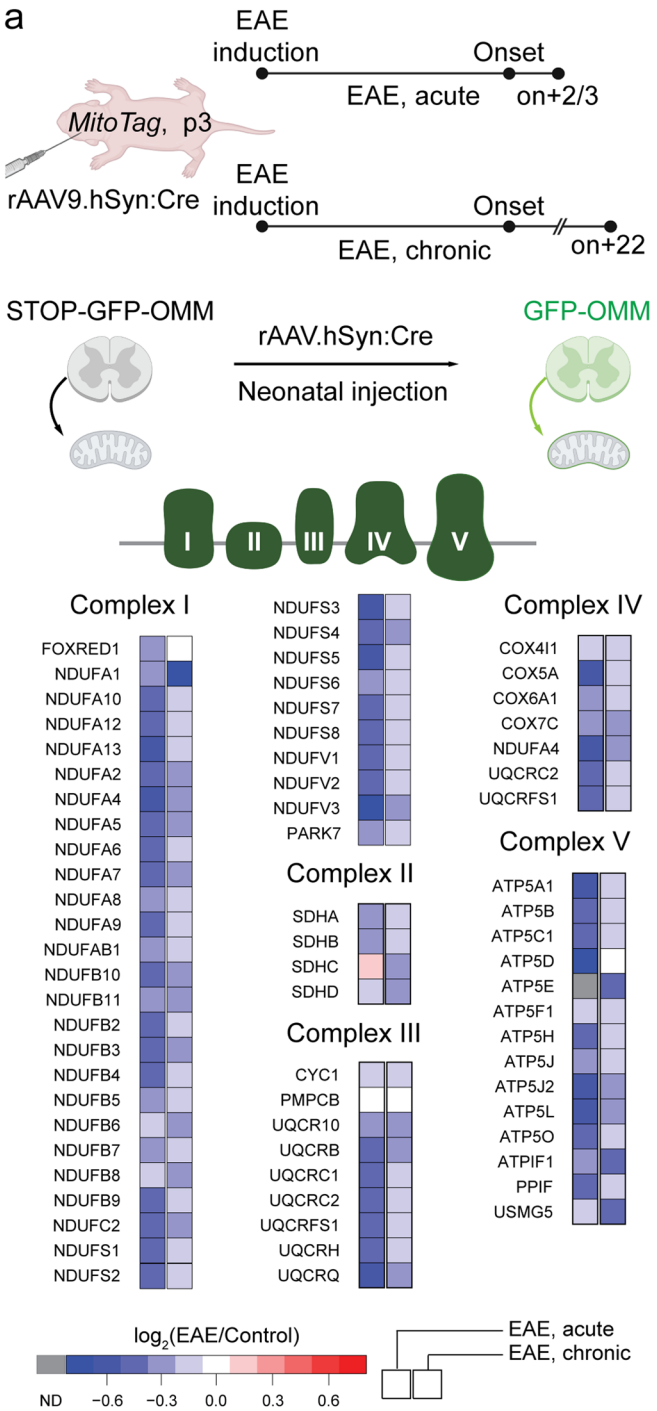

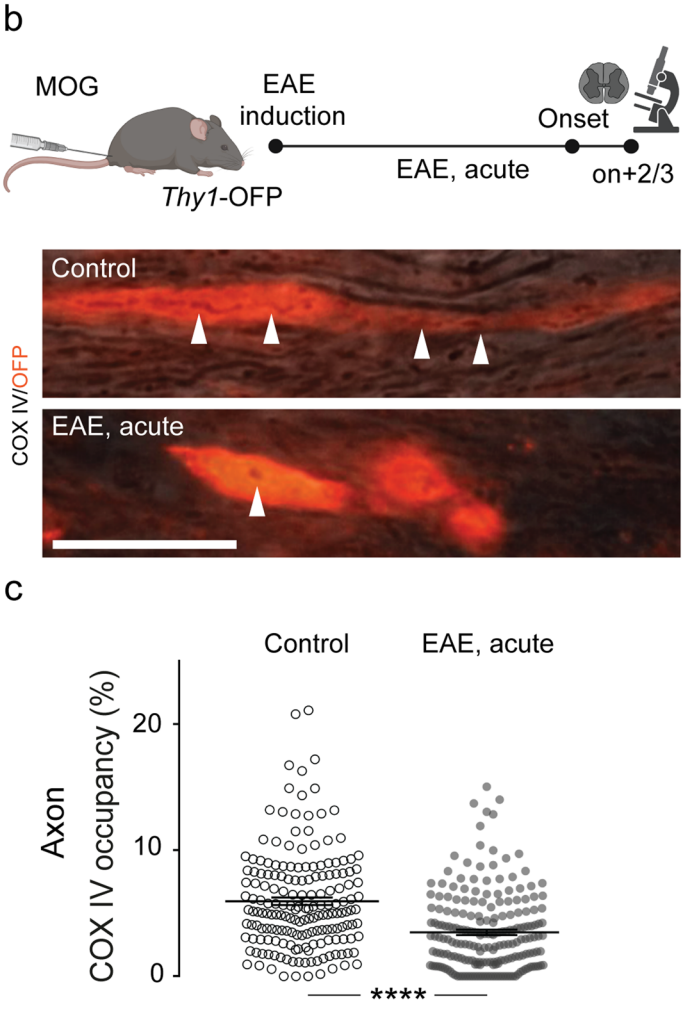

Extended Data Fig. 4 | Expression of ETC components in EAE neurons. (**a**) Top: Schematic of the experiment, analysis of same data sets as shown in Fig. 3. Bottom: Relative abundance of individual ETC complex components in neuronal mitochondria. Average shown as color-coded $\log_2$(EAE/Control) for acute and chronic EAE compared to respective controls. (**b**) *In situ* analysis of axonal COX IV activity using *in situ* histochemical assay in *Thy1*-OFP EAE spinal cords. Top: Schematic of the experiment. Bottom: Confocal image of control and EAE stage 1 axons, OFP (red) and COX IV (arrow heads indicate mitochondria as dark areas, as fluorescence of OFP is quenched by reaction product of COX IV assay). (**c**) Quantification of COX IV activity signal's occupancy of OFP axon area on axonal level. Mean ± s.e.m.; n = 180 axons from nine mice for control and 208 axons from nine mice for EAE using a two-tailed, Mann-Whitney test, $p = 5.2 \times 10^{-12}$. Scale bar: 25 µm in b. ****, $p < 0.001$. See source data for individual data points and further statistical parameters. Illustration created with BioRender.

https://doi.org/10.1038/s42255-023-00838-3

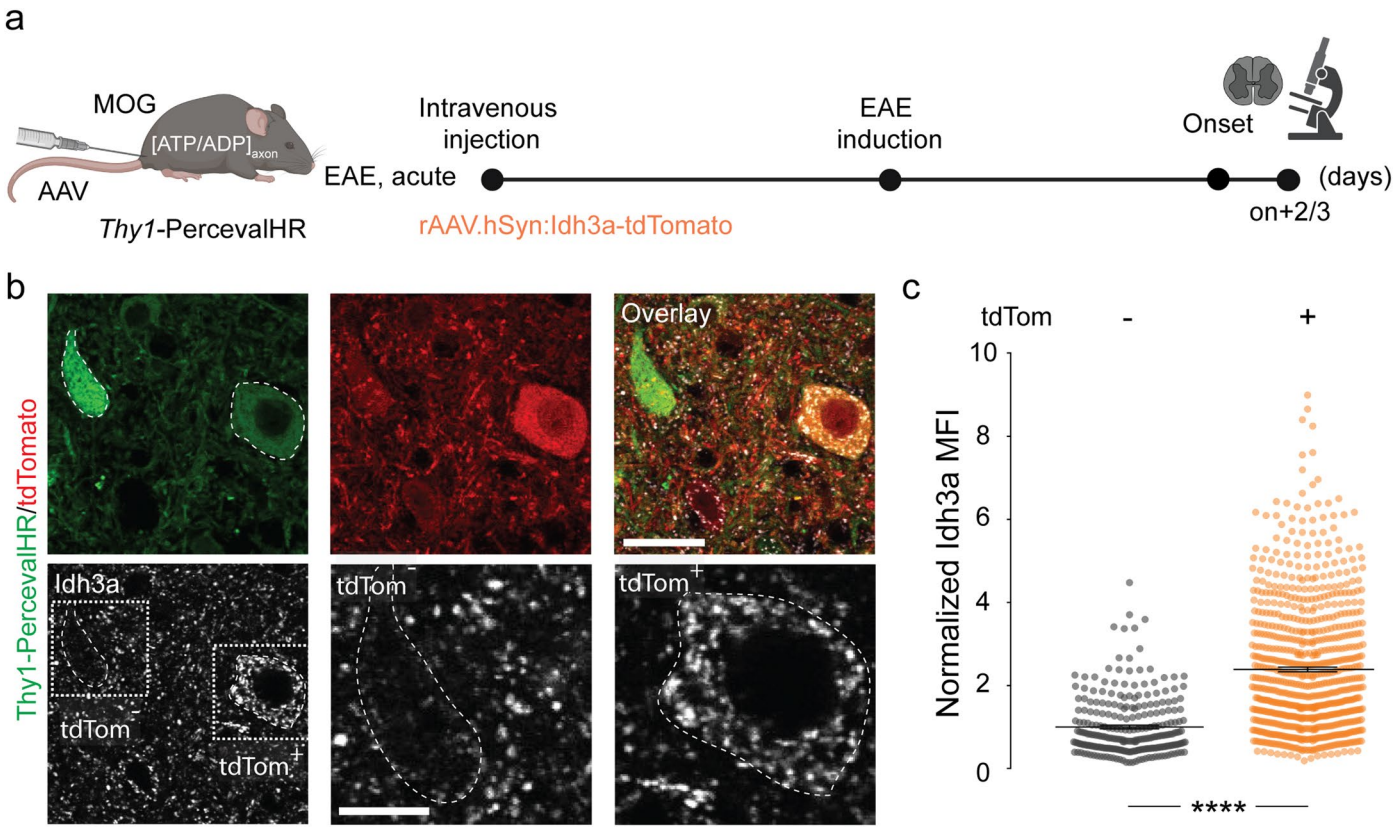

Extended Data Fig. 5 | Viral overexpression of Idh3a in EAE neurons. (**a**) Schematic of experiment, analysis of same data sets as shown in Fig. 6. (**b**) Confocal images of spinal cord sections of a *Thy1*-PercevalHR mouse (green) that was injected with rAAV.hSyn:Idh3a-tdTomato (tdTomato, tdTom, red). Bottom row shows immunostainings for Idh3a, with details highlighting, left, a tdTomato-negative ($tdTom^-$) and, right, a tdTomato-positive ($tdTom^+$) neuron with Idh3a overexpression. (**c**) Expression level of Idh3a in tdTomato-negative ($tdTom^-$) and tdTomato-positive ($tdTom^+$) neurons (mean ± s.e.m.; n = 266 $tdTom^-$ neurons and 803 $tdTom^+$ neurons using two-tailed, Mann-Whitney test, $p < 0.001$). Scale bar: 25 µm (top) and 10 µm (bottom) in b. ****, $p < 0.001$. See source data for individual data points and further statistical parameters. Illustration created with BioRender.

https://doi.org/10.1038/s42255-023-00838-3

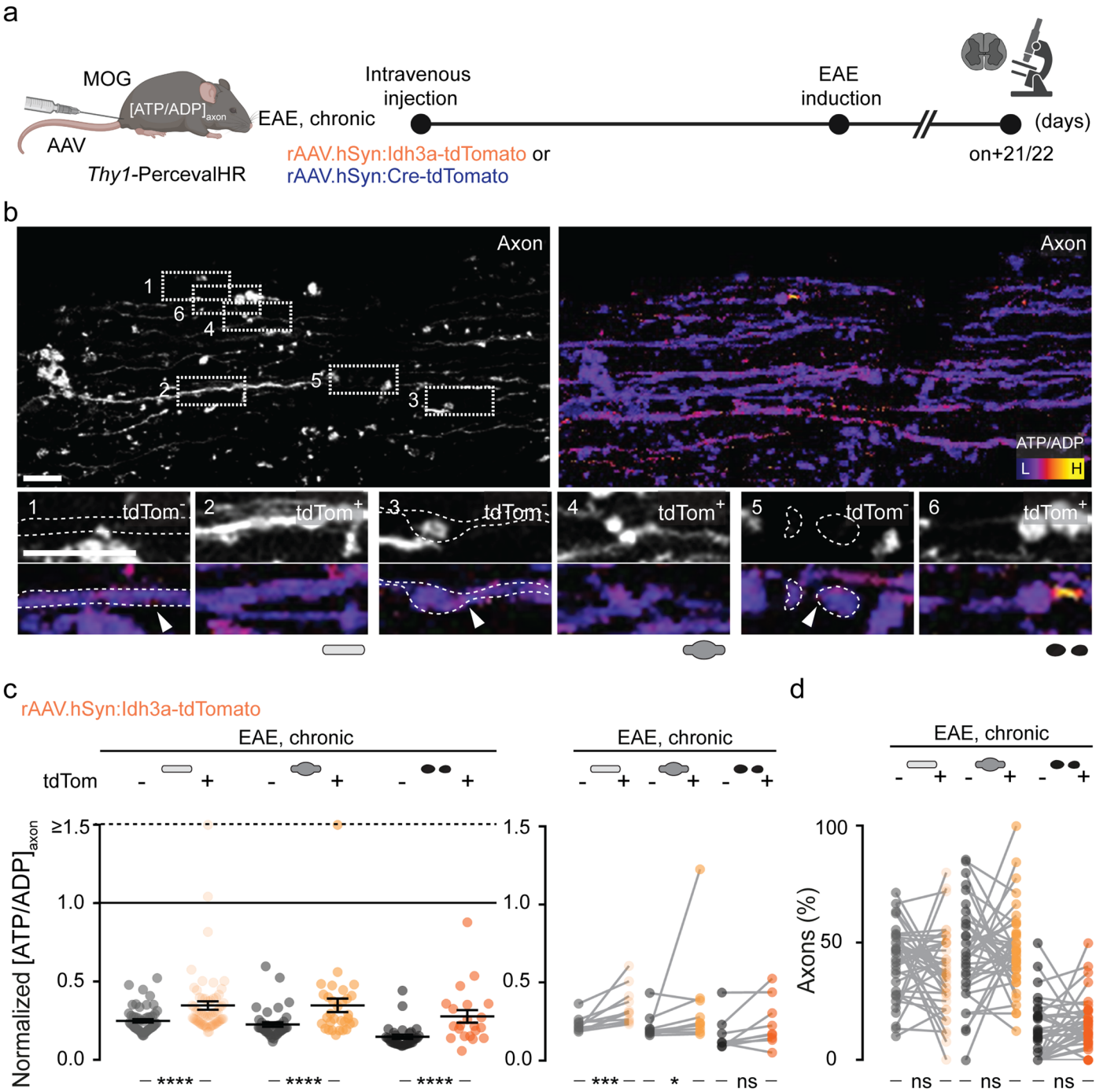

Extended Data Fig. 6 | Chronic Idh3 overexpression modestly ameliorates axonal ATP deficits in EAE lesions. (**a**) Experimental design for $[ATP/ADP]_{axon}$ measurements in chronic EAE in *Thy1*- PercevalHR mice virally overexpressing Idh3a or a control protein (Cre recombinase) and tdTomato in a subset of axons. (**b**) *In vivo* multi-photon image projections of chronically Idh3a-overexpressing *Thy1*-PercevalHR spinal axons. Left: Grayscale LUT of tdTomato. Right: Ratiometric $[ATP/ADP]_{axon}$ LUT (λ_{ex} ratio 950 nm/840 nm). Details: Image pairs of tdTomato-negative ($tdTom^-$; left) and -positive ($tdTom^+$; right) normal-appearing, swollen, and fragmented axons. (**c**) Comparison of $[ATP/ADP]_{axon}$ in $tdTom^-$ and $tdTom^+$ axons (λ_{ex} ratio 950 nm/840 nm, normalized to control axon mean indicated by black line; values above 1.5 lined up on the "≥1.5" dashed line). Left: $[ATP/ADP]_{axon}$ of single $tdTom^-$ (gray) and $tdTom^+$ (orange) axons. Right: Lesion-specific paired analysis of mean $[ATP/ADP]_{axon}$ in $tdTom^-$ (gray) and $tdTom^+$ (orange) axon populations of the three morphological stages. Mean ± s.e.m. Comparison of 130 $tdTom^-$ versus 115 $tdTom^+$ axons in 12 lesions from four mice in c using two-tailed, unpaired Student's t-test or Mann-Whitney test where normal distribution could not be confirmed (c, left graphs; $p = 7 \times 10^{-6}$, 9.9×10^{-5} and 3.8×10^{-5} for stages 0, 1 and 2) and a paired t-test (right graph; 0.001, 0.0273 and 0.0547 for stages 0, 1 and 2.) (**d**) Paired analysis of the frequency of stage 0, 1 and 2 in $tdTom^-$ (gray) and $tdTom^+$ (orange) axon populations. Mean ± s.e.m. Comparison of 551 $tdTom^-$ versus 539 $tdTom^+$ axons in 38 lesions from six mice in d using two-tailed, paired Student's t-test or Wilcoxon test where normal distribution could not be confirmed ($p = 0.2108$, 0.743 and 0.0575 for stage 0, 1 and 2). Scale bars: 25 µm in b. *, $p < 0.05$; ***, $p < 0.005$; ****, $p < 0.001$. See source data for individual data points and further statistical parameters. Illustration created with BioRender.

https://doi.org/10.1038/s42255-023-00838-3

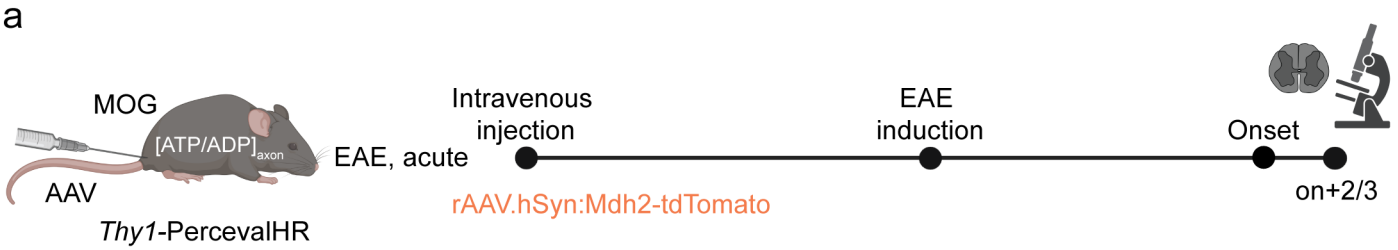

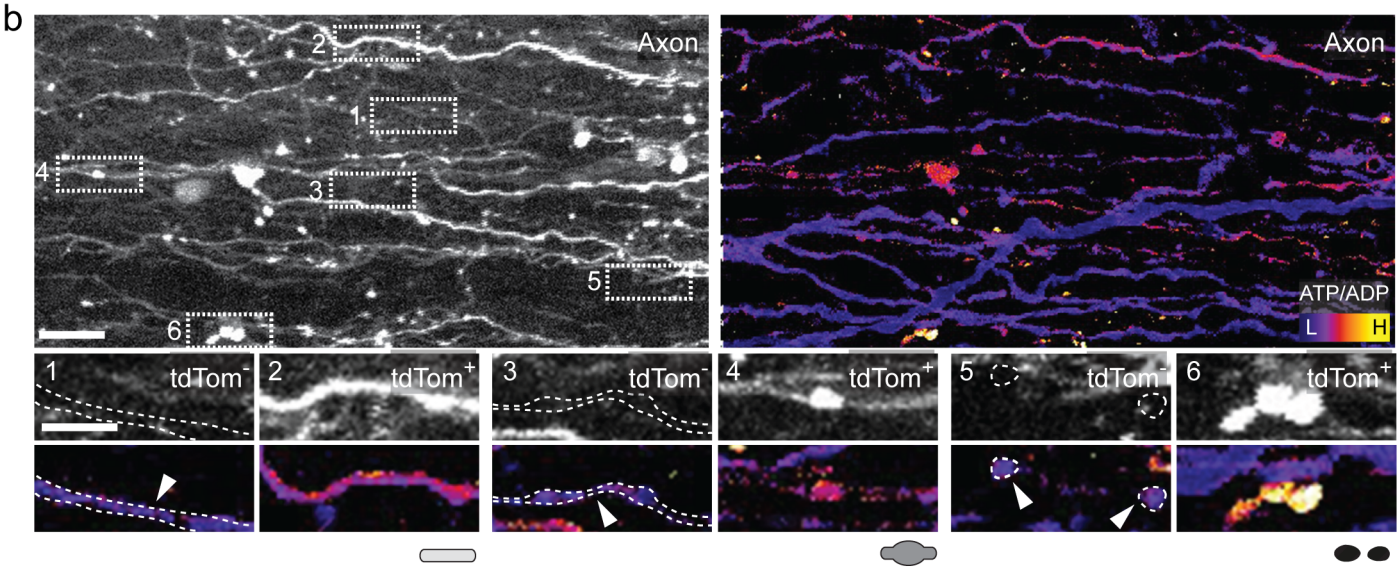

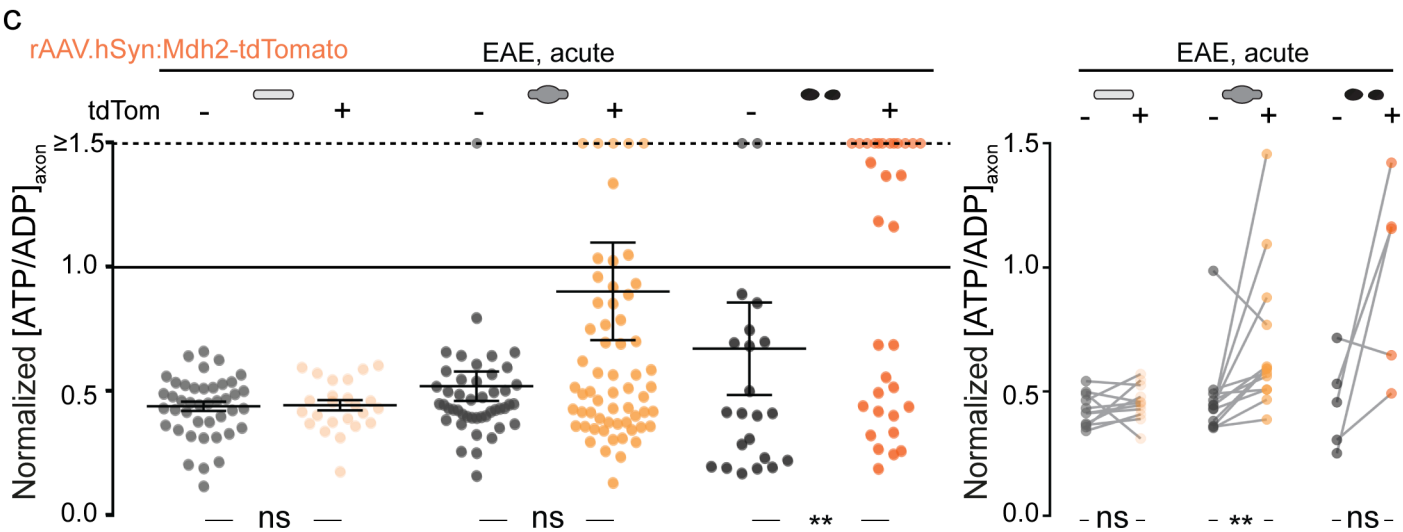

Extended Data Fig. 7 | Mdh2 overexpression ameliorates axonal ATP deficits in EAE lesions. (**a**) Experimental design for $[ATP/ADP]_{axon}$ in acute EAE in *Thy1*-PercevalHR mice that virally overexpressed Mdh2 together with tdTomato in a subset of axons. (**b**) Maximum intensity projections of *in vivo* multi-photon image stacks of spinal cord axons in Mdh2-overexpressing *Thy1*-PercevalHR mice. Left: Grayscale LUT of tdTomato. Right: Ratiometric $[ATP/ADP]_{axon}$ LUT (λ_{ex} ratio 950 nm/840 nm). Details show image pairs of tdTomato-negative (left) and -positive (right) normal-appearing, swollen, and fragmented axons in acute EAE. (**c**) Comparison of $[ATP/ADP]_{axon}$ in tdTomato-positive ($tdTom^+$) and -negative ($tdTom^-$) axons (plotted as λ_{ex} ratio 950 nm/840 nm, normalized to control axon mean indicated as the black line; values above 1.5 lined up on the "≥1.5" dashed line). Left: $[ATP/ADP]_{axon}$ of single $tdTom^-$ (gray) and $tdTom^+$ (orange) axons in Mdh2-overexpressing EAE mice, mean ± s.e.m. of $tdTom^+$ stage 2 axons are above 1.5. Right: Lesion-specific paired analysis of mean $[ATP/ADP]_{axon}$ in $tdTom^-$ (gray) and $tdTom^+$ (orange) axon populations of the three morphological stages. Mean ± s.e.m. Comparison of 110 $tdTom^-$axons versus 112 $tdTom^+$ axons in 14 lesions from four mice in using two-tailed, unpaired Student's t-test or Mann-Whitney test where normal distribution could not be confirmed (left graph; p = 0.8851, 0.1804 and 0.0039 for stage 0, 1 and 2, respectively) and a paired t-test or Wilcoxon test where normal distribution could not be confirmed (right graph; 0.3225, 0.004 and 0.0609 for stage 0, 1 and 2, respectively). Scale bar: 25 µm in b. **, $p < 0.01$. See source data for individual data points and further statistical parameters. Illustration created with BioRender.

https://doi.org/10.1038/s42255-023-00838-3

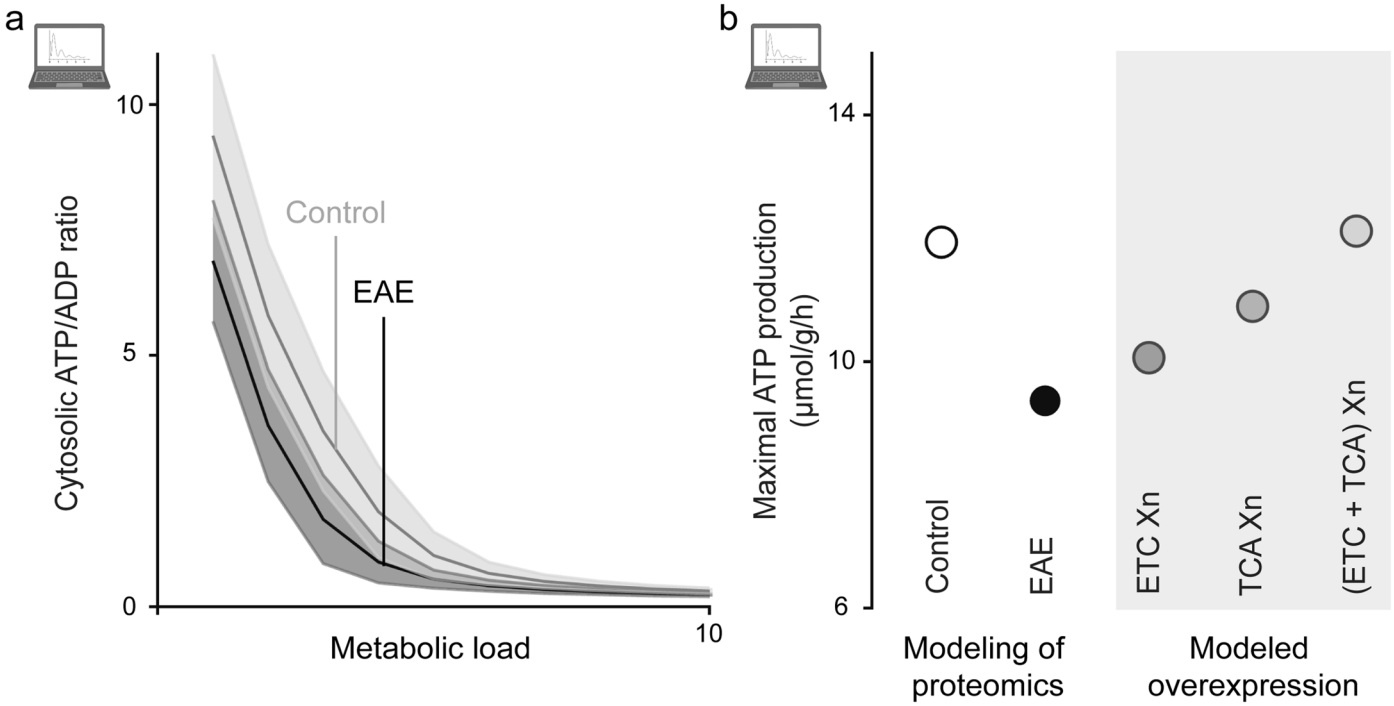

Extended Data Fig. 8 | Prediction of energy state using QSM™-based metabolic profiling. (a) Comparisons of predicted maximal ATP production based on AAV/*MitoTag*-based proteomic analysis in control, EAE, modeled overexpression (Xn) of ETC, TCA cycle and both ETC and TCA cycle. (b) Predicted cytosolic ATP/ADP ratio with increasing metabolic load in EAE (dark gray) compared to healthy control (light gray). See source data for individual data points and further statistical parameters. Illustration created with BioRender.

https://doi.org/10.1038/s42255-023-00838-3

Extended Data Table 1 | Information on human tissue samples used in this study

Case	Age	Sex	Histological specimen	State
MS1	41	female	Frontal lobe, subcortical lesion	Chronic active
MS3	45	female	Frontal lobe, subcortical lesion	Chronic active
MS4	51	female	Right frontal-parietal -lobe	Chronic active
MS5	55	male	Left frontal lobe	Chronic active
MS6	58	male	Frontal lobe, subcortical lesion	Chronic
MS8	25	female	Frontal lobe, subcortical lesion	Acute active
MS10	77	female	Not indicated	Acute active

nature portfolio

Corresponding author(s): Thomas Misgeld/ Martin Kerschensteiner

Last updated by author(s): May 22, 2023

Reporting Summary

Nature Portfolio wishes to improve the reproducibility of the work that we publish. This form provides structure for consistency and transparency in reporting. For further information on Nature Portfolio policies, see our Editorial Policies and the Editorial Policy Checklist.

Statistics

For all statistical analyses, confirm that the following items are present in the figure legend, table legend, main text, or Methods section.

n/a	Confirmed	
☐	☒	The exact sample size (*n*) for each experimental group/condition, given as a discrete number and unit of measurement
☐	☒	A statement on whether measurements were taken from distinct samples or whether the same sample was measured repeatedly
☐	☒	The statistical test(s) used AND whether they are one- or two-sided *Only common tests should be described solely by name; describe more complex techniques in the Methods section.*
☐	☒	A description of all covariates tested
☐	☒	A description of any assumptions or corrections, such as tests of normality and adjustment for multiple comparisons
☐	☒	A full description of the statistical parameters including central tendency (e.g. means) or other basic estimates (e.g. regression coefficient) AND variation (e.g. standard deviation) or associated estimates of uncertainty (e.g. confidence intervals)
☐	☒	For null hypothesis testing, the test statistic (e.g. *F*, *t*, *r*) with confidence intervals, effect sizes, degrees of freedom and *P* value noted *Give P values as exact values whenever suitable.*
☒	☐	For Bayesian analysis, information on the choice of priors and Markov chain Monte Carlo settings
☒	☐	For hierarchical and complex designs, identification of the appropriate level for tests and full reporting of outcomes
☒	☐	Estimates of effect sizes (e.g. Cohen's *d*, Pearson's *r*), indicating how they were calculated

Our web collection on statistics for biologists contains articles on many of the points above.

Software and code

Policy information about availability of computer code

Data collection	Olympus MPE-RS, Olympus FV1200 MPE and Olympus FV1000 confocal microscopy system were used for in vivo imaging. Olympus FV10-ASW (version 4.2) confocal microscopy system and Leica SP8 confocal microscopy system were used for in situ experiments. Zeiss Imager Z1 Apotome 2 microscope was used for COX histochemsitry analysis. 3DHistech Pannoramic P250 II whole slide scanner was used for human sections. Thermo Fisher Scientific Q-Exactive HF mass spectrometer coupled with Easy nLC-1200 nano UHPLC was used for mass spectrometry.
Data analysis	Open source software: ImageJ/Fiji (version 1.51u) for processing of images; GraphPad (version 7) for statistics and figure representation; Microsoft Excel 2022 for statistics; MaxQuant (Version 1.6.3.3 or 1.6.10.43) for processing of mass spectrometry; Reactome (version 7.4) for proteomics pathways analysis; R studio (version 4.2.2) and Python (version 3) package nezzworker for proteomics data processing; Adobe Photoshop CS6 for image processing; Adobe Illustrator CS6 for figure representation; SlideViewer software (v2.3, 3DHistech), Definiens Developer XD (version 2.7) and Visiopharm (version 2021.09) for human image analysis; QSM™ data analysis platform for metabolic modelling; Biorender for illustration display.

For manuscripts utilizing custom algorithms or software that are central to the research but not yet described in published literature, software must be made available to editors and reviewers. We strongly encourage code deposition in a community repository (e.g. GitHub). See the Nature Portfolio guidelines for submitting code & software for further information.

Data

Policy information about availability of data

All manuscripts must include a data availability statement. This statement should provide the following information, where applicable:

- Accession codes, unique identifiers, or web links for publicly available datasets
- A description of any restrictions on data availability
- For clinical datasets or third party data, please ensure that the statement adheres to our policy

All proteomic dataset generated within this study are deposited online to the ProteomeXchange Consortium via the PRIDE partner repository with the dataset identifier PXD032363 and at github (https://github.com/engelsdaniel/mitoproteomics). The codes used to reanalyze the single-cell data from Schattling et al. and the halflives data from Fornasiero et al. are publicly available on the github (https://github.com/engelsdaniel/mitoproteomics). Source data files for Figures and Extended Data Figures are provided with this paper. All additional data that support the findings of this study are available upon reasonable request to the corresponding authors. The transgenic mouse lines (Thy1-mitoTwitch2b and Thy1-PercevalHR) and the plasmids (pAAV.hSyn.Idh3a.p2a.tdTomato, pAAV.hSyn.Mdh2.p2a.tdTomato, pAAV.hSyn.Cre.p2a.tdTomato, pAAV.hSyn.Ateam1.03 and pAAV.hSyn.SypHer3s) are available upon request.

Research involving human participants, their data, or biological material

Policy information about studies with human participants or human data. See also policy information about sex, gender (identity/presentation), and sexual orientation and race, ethnicity and racism.

Reporting on sex and gender	5 female and 2 male patients
Reporting on race, ethnicity, or other socially relevant groupings	N/A
Population characteristics	25-77 years of age Diagnostics: multiple sclerosis
Recruitment	Samples were composed of tissues derived from two primary sources: autopsies and biopsies, primarily carried out in a diagnostic context, without pro-active recruitment of patients for this study, and samples were gathered based on the patient's prior consent or appropriate legal permission to use tissues for research purposes. Together this makes a self-selection bias less likely to affect the observed results.
Ethics oversight	The Use of human samples was in accordance with institutional ethical guidelines and approved by the ethics committee of the University of Geneva (Switzerland).

Note that full information on the approval of the study protocol must also be provided in the manuscript.

Field-specific reporting

Please select the one below that is the best fit for your research. If you are not sure, read the appropriate sections before making your selection.

☒ Life sciences ☐ Behavioural & social sciences ☐ Ecological, evolutionary & environmental sciences

For a reference copy of the document with all sections, see nature.com/documents/nr-reporting-summary-flat.pdf

Life sciences study design

All studies must disclose on these points even when the disclosure is negative.

Sample size	Although no power calculation was performed prior to study design to predetermine the sample sizes, the number of mice used ensured statistically relevant results are comparable to those reported in previous publications using similar experimental design (see Ref: Nikic et al., Nature Medicine 2011; Sorbara et al., Neuron 2014; Witte et al., Neuron 2019; Fecher et al., Nature Neuroscince 2019) All number of mice and cells are reported in the respective sections (i.e. Figure Legends, Online methods and source data files).
Data exclusions	Pre-established exclusion criteria were used in this study- animals showing signs of traumatic damage after laminectomy were excluded from the analysis based on the animal protocol. Mice or tissue showing insufficient labeling or staining, or structures showing insufficient signal to noise ratios were not analyzed; no other data points were excluded.
Replication	All animal experiments in this study include at least three biological replicates. The number of replicates is mentioned for each experiment in the figure legend. All attempts at replication were successful, except when the data exclusion criteria were met prior to analysis.
Randomization	Female and male were equally allocated into control and experimental groups if not explicitly mentioned otherwise (sample collection for mass spectrometry/ proteomics analysis in particular, only male mice were used). The experiments were not powered for independent analysis of male and female mice, but separate analysis of female and male mice did not reveal any major sex-specific effects in our analyses of ATP/ADP levels.

Blinding	Data collection and analysis was performed blind for figure 4 and figure 6 to avoid the selection bias. Others were not applied due to the nature of the binary type of experiment (obvious disease phenotype: control vs EAE). All analysis were performed using images displayed on a gray scale to avoid color-driven analysis bias.

Reporting for specific materials, systems and methods

We require information from authors about some types of materials, experimental systems and methods used in many studies. Here, indicate whether each material, system or method listed is relevant to your study. If you are not sure if a list item applies to your research, read the appropriate section before selecting a response.

Materials & experimental systems

n/a	Involved in the study
☐	☒ Antibodies
☐	☒ Eukaryotic cell lines
☒	☐ Palaeontology and archaeology
☐	☒ Animals and other organisms
☒	☐ Clinical data
☒	☐ Dual use research of concern
☒	☐ Plants

Methods

n/a	Involved in the study
☒	☐ ChIP-seq
☒	☐ Flow cytometry
☒	☐ MRI-based neuroimaging

Antibodies

Antibodies used	or tissue staining: Primary antibodies: Idh3a, Novus Biologicals, NBP1-32396; Dilution: IF - 1: 400 Idh2, Thermo Scientific, 702713; Dilution: IF - 1: 400 Mdh2, Novus Biologicals, NBP1-32259; Dilution: IF - 1 : 400 RFP, Novus Biologicals, NBP1-97371 ; Dilution: IF - 1: 1000 GFP, Abcam, ab13970; Dilution: IF - 1: 1000 NeuN, clone A60, Sigma, MAB377; Dilution: IF - 1: 400 Secondary antibodies: Anti-chicken IgY-Alexa Fluor 488, Thermo Scientific, A-11039; Dilution: IF - 1: 1000 Anti-rabbit IgG-Alexa Fluor 488, Thermo Scientific, A32731; Dilution: IF - 1 : 1000 Anti-mouse IgG-Alexa Fluor 594, Thermo Scientific , A-21125; Dilution: IF - 1: 1000 Anti-rabbit IgG-Alexa Fluor 594, Thermo Scientific, A-11012; Dilution: IF - 1: 1000 For mitochondrial isolation: Mouse IgG1-APC, Miltenyi Biotec, 130-113-758
Validation	All antibodies used in this study were commercially available and validated by the manufacturers or used in previous studies: Idh3a, Novus Biologicals, NBP1-32396 : Data sheet Idh2, Thermo Scientific, 702713 : RRID:AB_2734812; Data sheet Mdh2, Novus Biologicals, NBP1-32259 : Data sheet (The staining of Idh3a, Idh2 and Mdh2 were performed on tissues from Thy1-mitoRFP mice, where analysis can be restricted to red fluorescent protein (RFP)-tagged neuronal mitochondria.) RFP, Novus Biologicals, NBP1-97371 : Data sheet; 5 citations (PMID: 30159312/PMID: 30158698) GFP, Abcam, ab13970 : Data sheet (ab13970 staining GFP in GFP-transfected NIH/3T3cells.); 2965 citations NeuN, Sigma, MAB377 : Data sheet; 4999 citations (PMID: 31100147/PMID: 31474560) Anti-chicken IgY-Alexa Fluor 488, Thermo Scientific , A-11039 : RRID:AB_2534096; 168 citations Anti-rabbit IgG-Alexa Fluor 488, Thermo Scientific, A32731 : RRID:AB_2633280; 414 citations Anti-mouse IgG1-Alexa Fluor 594, Thermo Scientific, A-21125 : RRID:AB_2535767; 22 citations Anti-rabbit IgG-Alexa Fluor 594, Thermo Scientific , A-11012 : RRID:AB_2534079; 215 citations Mouse IgG1-APC, Miltenyi Biotec, 130-113-758 : RRID:AB_2733439; Ref: doi: 10.1016/j.ab.2009.02.040

Eukaryotic cell lines

Policy information about cell lines and Sex and Gender in Research

Cell line source(s)	HEK293T, ATCC, crl-3216.
Authentication	None of the cell lines used were authenticated.
Mycoplasma contamination	We confirm that all cell lines were tested negative for mycoplasma contamination.
Commonly misidentified lines (See ICLAC register)	N/A

Animals and other research organisms

Policy information about studies involving animals; ARRIVE guidelines recommended for reporting animal research, and Sex and Gender in Research

Laboratory animals	All experiments were performed on either postnatal day 3 pups or adult (age from 2 to 6 months) mice according to the protocols on a C57BL/6 (strain designation C57BL/6J, Jackson Laboratories) background, crossbred in our animal facilities. The following transgenic animals were used: Thy1-mitoGrx-roGFP x Thy1-OFP mice Thy1-PercevalHR Thy1-mitoTwitch2b x Thy1-OFP Rosa26-MitoTag Thy1-mitoRFP mice Thy1-OFP
Wild animals	Study did not involve any wild animals.
Reporting on sex	Both sexes were used and separate analysis of female and male mice did not reveal any major sex-specific effects (in our analyses of ATP/ADP levels). Exclusively, only male mice were used in the mass spectrometry/ proteomics analysis.
Field-collected samples	No field-collected animals were used in the study.
Ethics oversight	All animal experiments were performed in accordance with regulations of the relevant animal welfare acts and protocols approved by the local animal ethics committee of the state of Bavaria (Regierung von Oberbayern) in accordance with European guidelines.

Note that full information on the approval of the study protocol must also be provided in the manuscript.